Comparison of Disdrometer and X-Band Mobile Radar Observations in Convective Precipitation

EVAN A. KALINA AND KATJA FRIEDRICH

Department of Atmospheric and Oceanic Sciences, University of Colorado Boulder, Boulder, Colorado

SCOTT M. ELLIS

National Center for Atmospheric Research, Boulder, Colorado

DONALD W. BURGESS

Cooperative Institute for Mesoscale Meteorological Studies, University of Oklahoma, and National Severe Storms Laboratory, Norman, Oklahoma

(Manuscript received 28 January 2014, in final form 11 March 2014)

ABSTRACT

Microphysical data from thunderstorms are sparse, yet they are essential to validate microphysical schemes in numerical models. Mobile, dual-polarization, X-band radars are capable of providing a wealth of data that include radar reflectivity, drop shape, and hydrometeor type. However, X-band radars suffer from beam attenuation in heavy rainfall and hail, which can be partially corrected with attenuation correction schemes. In this research, the authors compare surface disdrometer observations to results from a differential phase-based attenuation correction scheme. This scheme is applied to data recorded by the National Oceanic and Atmospheric Administration (NOAA) X-band dual-polarized (NOXP) mobile radar, which was deployed during the second Verification of the Origins of Rotation in Tornadoes Experiment (VORTEX2). Results are presented from five supercell thunderstorms and one squall line (183 min of data). The median disagreement (radar–disdrometer) in attenuation-corrected reflectivity Z and differential reflectivity Z_{DR} is just 1.0 and 0.19 dB, respectively. However, two data subsets reveal much larger discrepancies in Z (Z_{DR}): 5.8 (1.6) dB in a hailstorm and −13 (−0.61) dB when the radar signal quality index (SQI) is less than 0.8. The discrepancies are much smaller when disdrometer and S-band Weather Surveillance Radar-1988 Doppler (WSR-88D) Z are compared, with differences of −1.5 dB (hailstorm) and −0.66 dB (NOXP SQI < 0.8). A comparison of the hydrometeor type retrieved from disdrometer and NOXP radar data is also presented, in which the same class is assigned 63% of the time.

1. Introduction

The lack of surface microphysical and in situ data is a critical obstacle in our attempts to understand and model severe thunderstorms accurately. Microphysical processes (e.g., accretion, collision, coalescence, drop breakup, melting, and evaporation) affect storm behavior and evolution by serving as a crucial link between the storm dynamics and thermodynamics. For example, the melting of hail influences the strength and size of the low-level cold pool, which changes the near-surface buoyancy tendency and, as suggested by several recent studies, the tornadogenesis potential (Markowski et al. 2002; Shabbott and Markowski 2006; Grzych et al. 2007). To collect the surface microphysical data required to understand and quantify these interactions, Particle Size and Velocity (PARSIVEL) optical disdrometers were deployed during the second Verification of the Origins of Rotation in Tornadoes Experiment (VORTEX2) to obtain particle diameter and fall speed distributions in severe thunderstorms. For the first time, these deployments were coordinated with X-band, mobile, polarimetric Doppler radars in severe thunderstorms, which provided a three-dimensional dataset of radar reflectivity Z, differential reflectivity Z_{DR}, and

Corresponding author address: Evan A. Kalina, Department of Atmospheric and Oceanic Sciences, University of Colorado Boulder, UCB 311, Boulder, CO 80309.
E-mail: evan.kalina@colorado.edu

DOI: 10.1175/MWR-D-14-00039.1

differential phase Ψ_{DP} that is needed to characterize microphysical processes throughout thunderstorms.

The VORTEX2 measurements of supercell thunderstorm microphysics with disdrometers and mobile X-band radars are unprecedented, since both sets of instruments were deployed close to the storm and yielded high-resolution information near and at the surface. This dataset provides researchers with a unique opportunity to compare disdrometer data to output from hydrometeor classification schemes that are based on dual-polarization radar observations. However, the measurement accuracy of both instruments is strongly affected by the severe nature of the storms, which contain hail and strong winds. To combine in situ microphysical data at the surface with three-dimensional radar imagery, microphysical data need to be quality controlled and rain and hail particles must be discriminated. In addition, attenuation of the X-band radar signal must be corrected using algorithms that may be error prone, particularly when the radar samples mixed-phase precipitation. A proven algorithm to correct attenuation in hail does not yet exist (Borowska et al. 2011; Ryzhkov et al. 2013a), although recent efforts to develop a scheme valid in melting hail are presented in Ryzhkov et al. (2013a,b). Because supercell thunderstorms often contain large amounts of hail, attenuation correction schemes designed for rain will not always yield accurate results.

In this paper, we compare attenuation-corrected radar data and hydrometeor classifications to surface disdrometer measurements in supercell thunderstorms. Can disdrometer data be used to provide guidance on the performance of radar attenuation correction schemes, and therefore to provide a measure of radar data quality? To investigate, we first apply a quality-control algorithm and a hydrometeor classification scheme for in situ disdrometer data that uses the particle size and fall speed distributions from the disdrometer to classify particles as rain, small hail ($2 < d < 5$ mm), and large hail ($d > 5$ mm; note that in this study, "large" is simply relative to the small hail class and is not meant to be an argument against the typical definition of large hail of $d > 20$ mm). We then assess the performance of the attenuation correction scheme by comparing disdrometer-derived Z and Z_{DR} to X-band radar Z and Z_{DR} and to S-band radar Z. Comparisons between the disdrometer hydrometeor classification scheme and an existing scheme for X-band radar data are also provided.

A brief review of the different techniques that can be used to correct attenuation is now given. Several attenuation correction schemes use the propagation differential phase Φ_{DP} and specific differential phase K_{DP} to estimate the total and specific attenuation, respectively (e.g., Carey et al. 2000; Testud et al. 2000; Bringi et al. 2001; Anagnostou et al. 2006; Steiner et al. 2009). The quantity K_{DP} is the range derivative of Φ_{DP}, which must be calculated from the radar-measured total differential phase Ψ_{DP}. The Ψ_{DP} is the sum of Φ_{DP} and the backscatter differential phase δ. The terms Ψ_{DP}, Φ_{DP}, δ, and K_{DP} are related via Eq. (1):

$$2\int_0^r K_{DP}(r')\,dr' = \Psi_{DP} - \delta = \Phi_{DP}, \tag{1}$$

where r is the radar range. The quantity δ is only significant in the Mie scattering regime, which applies to rain drops with $d > 2.3$ mm at a temperature of 20°C at X band (Ryzhkov et al. 2011). Therefore, δ must be estimated before Φ_{DP} and K_{DP} can be used to correct the attenuation. Each attenuation correction scheme differs in the method used to calculate δ. Anagnostou et al. (2006) uses the differential reflectivity Z_{DR} in an iterative approach to estimate δ, while Steiner et al. (2009) applies the iterative, finite impulse response filter from Hubbert and Bringi (1995) to the measured Ψ_{DP} field. Once corrected Z, Z_{DR}, and K_{DP} are obtained, a fuzzy logic hydrometeor classification scheme [section 3b(2)] can be applied to the radar data to determine the dominant hydrometeor type observed in each range gate (Vivekanandan et al. 1999; Liu and Chandrasekar 2000; Iwanami et al. 2007; Park et al. 2009; Dolan and Rutledge 2009; Snyder et al. 2010).

To our knowledge, this study is one of the first to use disdrometer observations to analyze the performance of attenuation correction and hydrometeor classification schemes for X-band radar measurements in severe thunderstorms. Most previous studies that compared radar and disdrometer data developed empirical relationships between reflectivity and rainfall rate (e.g., Schuur et al. 2001; Ulbrich and Miller 2001; Bringi et al. 2003; Kanofsky and Chilson 2008; Huang et al. 2010). In addition, such studies have primarily been conducted in stratiform precipitation (e.g., Geotis 1978; Goddard et al. 1982; Thomson and List 1996; Zhang et al. 2011), while only a few comparisons have been performed in severe thunderstorms (Schuur et al. 2001; Thurai et al. 2010, 2011). X-band radar attenuation correction schemes have mostly been evaluated through comparison with S-band radar data, which are less attenuated (e.g., Anagnostou et al. 2006; Steiner et al. 2009; Snyder et al. 2010). Here, we propose an alternative method to evaluate attenuation correction schemes with surface disdrometer data. While we do not argue that this approach outperforms comparisons with S-band radar, the question remains whether disdrometers could be used if no nearby S-band radars are present. In addition, because the S-band Weather Surveillance Radar-1988

TABLE 1. Deployment details for the cases included in this analysis. All of the cases listed are supercell thunderstorms, except for the squall line of 12 Jun 2010.

Date	Times (UTC)	Location	Disdrometers	NOXP distance (km) (beam height, m)	WSR-88D distance (km) (beam height, km)
17 May	2218–2333	Artesia, NM	CU01, UF04–07	16–45 (280–920)	KFDX 200–207 (4.1–4.3)
19 May	2059–2122	Kingfisher, OK	CU01, UF01, UF05, UF07	29–38 (550–740)	KTLX 168–173 (3.1–3.3)
2 Jun	2320–2326	Benkelman, NE	UF03	23 (430)	KGLD 67 (0.85)
7 Jun	0005–0143	Mitchell, NE	CU01, UF01, UF05, UF07	30–37 (580–720)	KCYS 123–138 (2.0–2.3)
9 Jun	0118–0139	Scottsbluff, NE	CU01, UF01, UF03, UF05–06	24–27 (460–510)	KCYS 103–107 (1.5–1.6)
12 Jun	2100–2203	Gruver, TX	CU01, UF01, UF05–06	10–21 (190–390)	KAMA 111–113 (1.7)

Doppler (WSR-88D) dual-polarization upgrade was not complete in 2010, mobile radar Z_{DR} measurements corrected for differential attenuation and results from mobile radar hydrometeor classification algorithms cannot be validated with traditional S-band radar comparisons. Therefore, the goal of this study is to determine the relative quality of the VORTEX2 disdrometer and X-band radar data with the intention of improving the results from future observational analyses and numerical modeling studies that use these datasets for microphysical retrievals.

2. Cases, instruments, and data collection

a. Case selection

Coordinated radar and disdrometer data were obtained from ~36 severe thunderstorms during the second year of VORTEX2, a 12-week field campaign conducted in the Great Plains of the United States during May and June of 2009 and 2010 (Wurman et al. 2012). For this study, three criteria were used for case selection: 1) radar data above the disdrometer sites were available for at least 5 min, 2) the disdrometers observed $Z > 20$ dBZ (approximate threshold between drizzle and light rain; Rinehart 2004) for at least 5 min, and 3) the distance between the radar and the disdrometers was less than 45 km. Based on these criteria, we consider data from five supercell thunderstorms and one squall line (total of ~183 min of data). Table 1 provides details on the cases, and Fig. 1 shows examples of radar reflectivity from each case at an elevation angle of 1°.

b. Disdrometer measurements

The OTT PARSIVEL optical disdrometer (Löffler-Mang and Joss 2000) is an integrated laser transmitter–receiver that uses a 180-mm-long, 30-mm-wide, and 1-mm-thick light sheet to detect the diameter and fall speed of precipitation particles. More information about the measurement principle can be found in Löffler-Mang and Joss (2000), Löffler-Mang and Blahak (2001), Yuter et al. (2006), and references within. During VORTEX2, two types of disdrometers (Fig. 2) were deployed: articulating disdrometers (denoted as UF01 and UF03), with a measurement volume that was oriented continuously perpendicular to the 10-s running average of the particle trajectory of a 1.2-mm raindrop (Friedrich et al. 2013b), and stationary disdrometers (denoted as CU01, UF04, UF05, UF06, and UF07), with a measurement volume that remained fixed and parallel to the ground. For supercell thunderstorms, the disdrometers were deployed in advance of the southern side of the forward-flank downdraft (Fig. 3), with the mobile weather radars deployed to the southeast of the thunderstorm. The distance between the disdrometers and the radar ranged from 10 to 45 km, with a median distance of 20 km. Further details on the deployment strategy are provided in Friedrich et al. (2013b).

c. Radar measurements

Radar data were obtained from the National Oceanic and Atmospheric Administration (NOAA) X-band dual-polarized (NOXP) mobile radar (Palmer et al. 2009; Burgess et al. 2010). Table 2 provides a summary of the radar configuration during VORTEX2. For the cases considered in this research, the size of the radar resolution volume above the disdrometer sites ranged from 74 m × 87 m × 175 m at 10-km range to 74 m × 393 m × 785 m at 45-km range in range, azimuth, and height, respectively. The radar was electronically leveled, and a digital compass was used to record its heading. With respect to the location of the disdrometers, the height of the lowest radar beam ranged from 0.2 to 1 km AGL, but was mainly below 0.6 km AGL (Table 1).

3. Data processing

a. Disdrometer

1) QUALITY CONTROL AND HYDROMETEOR CLASSIFICATION SCHEME

A quality-control procedure (Fig. 4) was applied to the stationary and articulating disdrometer data to address

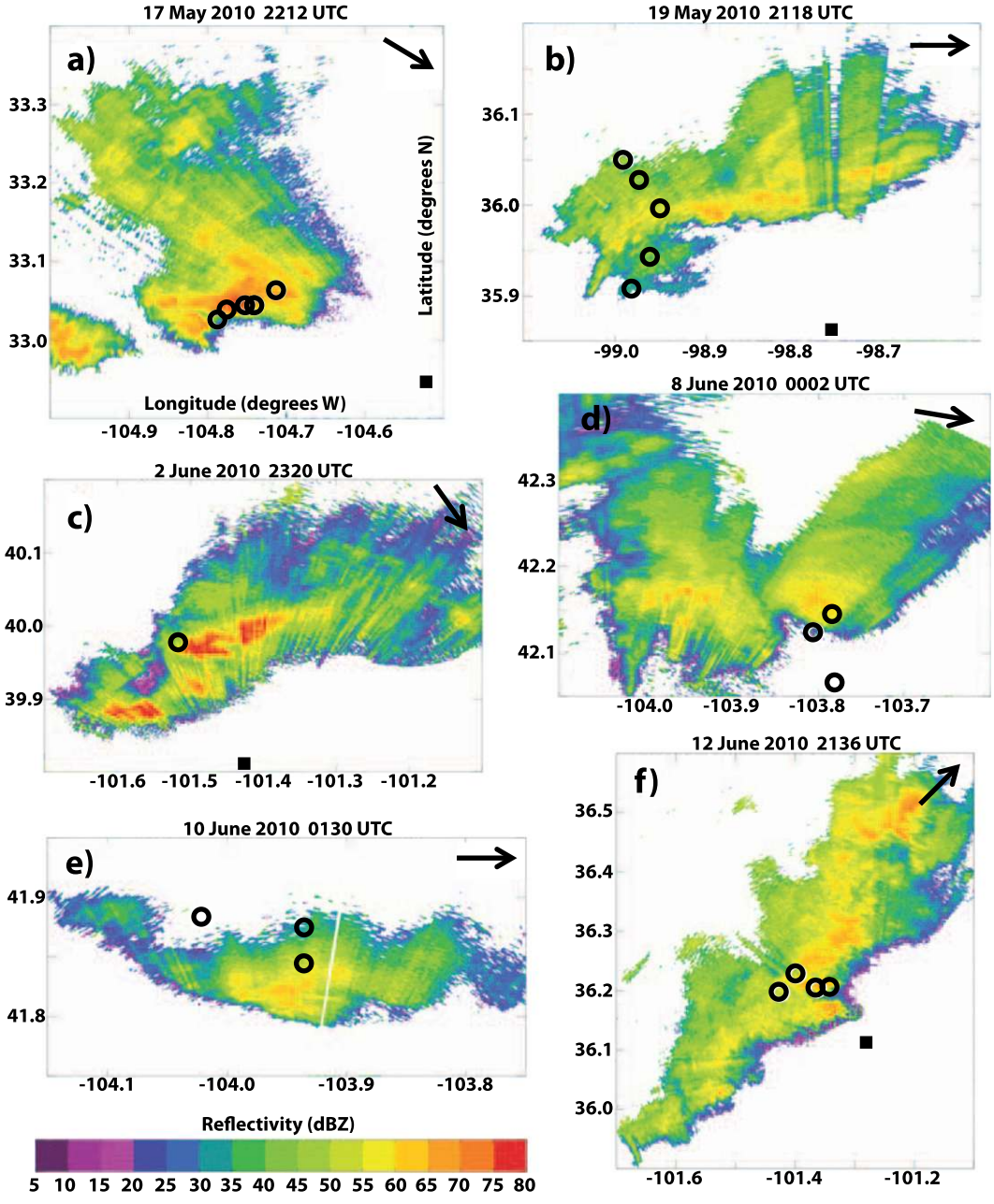

FIG. 1. Plan position indicator displays of attenuation-corrected radar reflectivity measured by NOXP at 1° elevation angle at (a) 2212 UTC 17 May 2010, (b) 2118 UTC 19 May 2010, (c) 2320 UTC 2 Jun 2010, (d) 0002 UTC 8 Jun 2010, (e) 0130 UTC 10 Jun 2010, and (f) 2136 UTC 12 Jun 2010. Disdrometer and radar locations are denoted by open circles and filled squares, respectively. The arrow shows the storm motion direction.

three documented error sources: strong winds, particles that only partially transect the sample volume (i.e., margin fallers), and splashing (e.g., Sevruk 1982; Illingworth and Stevens 1987; Nešpor et al. 2000; Schuur et al. 2001; Kruger and Krajewski 2002; Barthazy et al. 2004; Thurai and Bringi 2005; Yuter et al. 2006; Friedrich et al. 2013a). Friedrich et al. (2013a) analyzed wind-induced errors in PARSIVEL disdrometer data collected in a tropical cyclone and two supercell thunderstorms with wind speeds up to $30\,\mathrm{m\,s^{-1}}$, using six stationary and two articulating disdrometers. Misclassified particles, with $d > 5\,\mathrm{mm}$ and unphysically slow fall speeds ($v < 1\,\mathrm{m\,s^{-1}}$), were identified in the stationary (but not the articulating) disdrometer data at wind speeds as slow as $10\,\mathrm{m\,s^{-1}}$

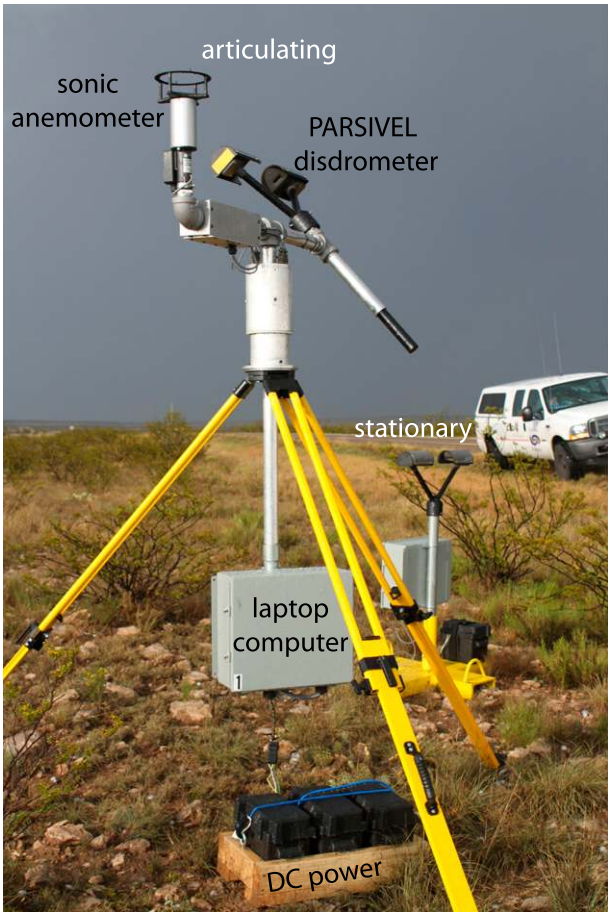

FIG. 2. A photograph of an articulating disdrometer (foreground) and a stationary disdrometer (background) deployed in Artesia, NM, on 17 May 2010.

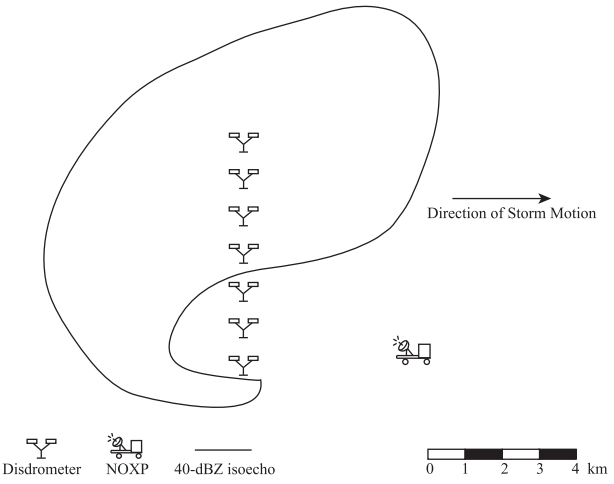

FIG. 3. An idealized schematic that shows the disdrometer and radar deployment strategy for supercell thunderstorms. The disdrometers were deployed in a line that was perpendicular to the storm motion vector with an instrument spacing of 0.2–1 km. The radar was deployed ahead of the forward-flank downdraft of the thunderstorm and was always within 45 km of the disdrometer deployments (ideally within 15 km). The location of the 40-dBZ isoecho is shown in black.

and were observed consistently at wind speeds larger than 20 m s^{-1}. To avoid misclassified particles in this analysis, we remove entire time steps in which the stationary disdrometers observed particles with $d > 5$ mm and slow fall speeds ($v < 1$ m s^{-1}). Second, margin fallers and splashing raindrops are removed from both types of disdrometer data by eliminating raindrops with a fall speed more than 60% faster or slower than the fall speed–diameter relationship for rain (Gunn and Kinzer 1949; Atlas et al. 1973), based on a study of PARSIVEL disdrometer accuracy by Jaffrain and Berne (2011).

The decision to classify a particle as rain, small hail, or large hail is based on its diameter and fall speed (Fig. 4). While the reader is referred to Friedrich et al. (2013b) for a detailed description of the classification scheme, two notes are merited here. First, we distinguish between small and large hail because small ice particles in thunderstorms are partially melted hailstones that consist of a torus of liquid water that surrounds an ice core (Rasmussen and Heymsfield 1987; Bringi and Chandrasekar 2001). Therefore, small and large hail need to be assigned different fractional water contents when the transition (T-) matrix method is used to compute the scattering properties of the particle size distribution [PSD; see section 3a(2) and Table 3]. Appendix A demonstrates that for the PSDs in this study, the sensitivity of disdrometer Z and Z_{DR} to the small hail fractional water content is less than 0.1 dB, because the small sample area of the PARSIVEL disdrometer captures relatively few hailstones. Second, while raindrop fall speed is a well-defined function of diameter (Gunn and Kinzer 1949; Atlas et al. 1973), the various shapes, densities, and water loadings of hail make it

TABLE 2. NOXP radar characteristics for the 2010 VORTEX2 field campaign.

Wavelength	3.21 cm (X band)
Transmission mode	Simultaneous transmission and reception (SHV)
Beamwidth	1°
Range resolution	74 m
Azimuthal resolution	0.5°
Elevation angles scanned	1° to ≤ 15° (1° increments)
Maximum unambiguous range	60.0 km
Nyquist velocity	19.9 m s^{-1}
Pulse repetition frequency	2500 Hz
Moments and variables	Reflectivity, Doppler velocity, spectrum width, differential reflectivity, differential phase, and correlation coefficient

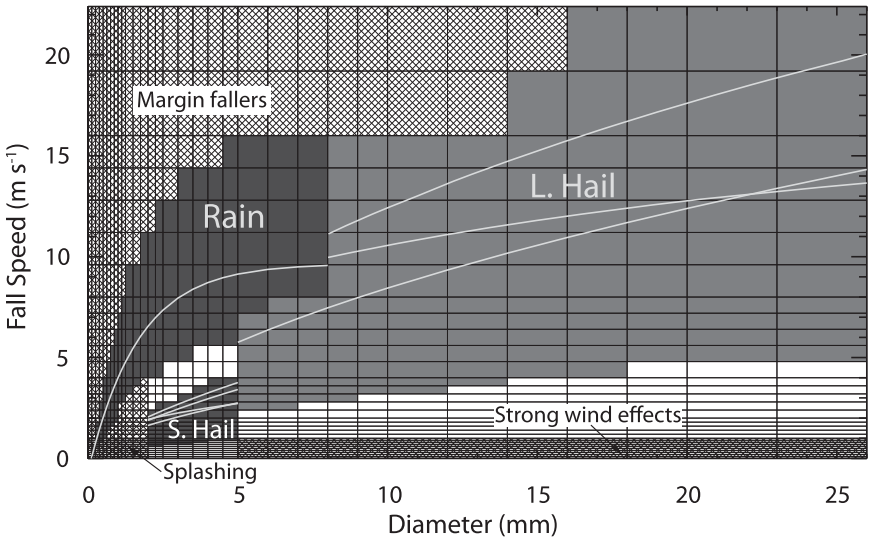

FIG. 4. Fall speed vs diameter plot depicting the quality-control procedures and the hydrometeor classification scheme applied to the disdrometer data [adapted from Fig. 5 in Friedrich et al. (2013b)]. The white solid lines in the rain, small hail, and large hail regions are the empirical diameter–fall speed relationships for rain (Atlas et al. 1973), graupel (Locatelli and Hobbs 1974), and hail (Knight and Heymsfield 1983), respectively.

possible for an ice particle to have a range of fall speeds for a given diameter, raising the possibility that a hail particle could be erroneously classified as rain. In addition, the disdrometer hydrometeor classification scheme (Fig. 4) uses the fall speed curves for dry graupel to define the small hail region, following Friedrich et al. (2013b). However, because the bulk density of small hail in thunderstorms exceeds that of graupel, the graupel fall speed relations are likely less than the fall speeds observed here. Therefore, some of the small hail may be detected in the unclassified region between the small hail and rain classes in Fig. 4. Because there is uncertainty over whether particles in this region are rain or small hail, these particles are left unclassified. Appendix B explores the sensitivity of the results to whether particles in the unclassified region are included in the analysis, revealing a mean sensitivity of ~0.2 dB in Z and 0.01 dB in Z_{DR} (relative to Z and Z_{DR} obtained by excluding the particles).

2) COMPUTATION OF METEOROLOGICAL VARIABLES FROM DISDROMETER DATA

Before calculating Z and Z_{DR} from the disdrometer data, number distributions were accumulated over periods of 60 s to obtain sufficiently large particle samples. The 60-s accumulation time causes higher-frequency variations in the PSD to be lost. These variations would likely be retained in the radar data due to the excellent range resolution (74 m), possibly causing the radar and disdrometer measurements to represent different PSDs (this issue is partially addressed by averaging the radar data; see section 3c). Next, the T-matrix method (Vivekanandan et al. 1991; Bringi and Chandrasekar 2001) was used to compute Z and Z_{DR} for each 60-s time

TABLE 3. Parameters used in the T-matrix program [i.e., canting angle (CA), axis ratio (AR), hydrometeor density (HD), fractional water content (FWC), and temperature (T)]. The mean and standard deviation are denoted by μ and σ, respectively. For comparison to NOXP radar (WSR-88D) data, calculations were performed at a radar frequency of 9.41 GHz (2.895 GHz) and a radar elevation angle of 1° (0.5°).

Hydrometeor	Parameters	References
Rain	CA: $\mu = 0°$, $\sigma = 7.5°$ T: 15°C	Huang et al. (2008)
Small hail	CA: $\mu = 0°$, $\sigma = 50°$	Snyder et al. (2010); Ryzhkov et al. (2011)
	AR: 0.8	Huang et al. (2005)
	HD: 0.9 g cm^{-3}	Vivekanandan et al. (1993)
	FWC: 0.5 T: 0°C	Huang et al. (2005)
Large hail	CA: $\mu = 0°$, $\sigma = 50°$	Snyder et al. (2010); Ryzhkov et al. (2011)
	AR: 0.8	Knight (1986); Balakrishnan and Zrnić (1990)
	HD: 0.9 g cm^{-3}	Vivekanandan et al. (1993); Solheim et al. (1999)
	FWC: 0.2 T: 0°C	Aydin et al. (1998)

step. Because the scattering properties of rain and ice particles differ, separate rain, small hail, and large hail distributions were input to the T-matrix program for each time step. For rain particles, the drop shape model from Beard and Chuang (1987) was chosen, which remains accurate at the large drop diameters present in convective weather (i.e., within ±4% of the measured axis ratios at $d > 5$ mm; Thurai et al. 2009). The raindrops were assumed to have a temperature of 15°C, a mean canting angle of 0°, and a canting angle standard deviation of 7.5° (Huang et al. 2008). Of these settings, Z and Z_{DR} display the greatest sensitivity to the canting angle standard deviation; however, the change in Z_{DR} is generally less than 0.1 dB across the range of physically reasonable values (1°–10°; Kwiatkowski et al. 1995). Hail particles were assumed to have a canting angle mean and standard deviation of 0° and 50°, respectively (Snyder et al. 2010; Ryzhkov et al. 2011), and were assigned a temperature of 0°C. The hailstones were modeled as a uniform mixture of ice and liquid water using the Maxwell–Garnett mixing formula, with ice (liquid water) as the matrix and liquid water (ice) as the inclusions in large (small) hailstones (Bringi and Chandrasekar 2001; Ryzhkov et al. 2011). Table 3 summarizes the parameters used in the T-matrix program for rain, small hail, and large hail.

b. Radar data processing

1) Radar attenuation correction scheme

The attenuation correction scheme from Steiner et al. (2009) is applied to the radar data. Steiner et al. (2009) evaluated the performance of this scheme with data that were collected in convective storms during the 2002 International H_2O Project (IHOP) by the National Observatory of Athens (NOA) X-band radar. For X-band radars with simultaneous horizontal and vertical polarization (SHV) transmit, attenuation correction in heavy rain was found to be most accurate when Z_{DR} was not used to estimate the attenuation or differential attenuation (Steiner et al. 2009). Potential biases in Z_{DR} caused by antenna and depolarization errors as Ψ_{DP} increases (Ryzhkov and Zrnić 2007; Hubbert et al. 2010a,b; Zrnić et al. 2010) are thereby avoided.

The Steiner et al. (2009) attenuation correction scheme is modified from the differential phase-based algorithm presented in Anagnostou et al. (2006). The first modification is that δ was removed from Ψ_{DP} with five iterations of the finite impulse response filter from Hubbert and Bringi (1995), rather than using Z_{DR} to estimate δ. The smoothed Φ_{DP} range profile was then used to estimate the path-integrated attenuation at horizontal polarization [Eq. (2)] and to correct Z_H [Eq. (3)]:

$$\mathrm{PIA}_H = \int_0^r A_H(r)\,dr = \gamma \times [\Phi_{DP}(r) - \Phi_{DP}(0)], \quad (2)$$

$$Z'_H = Z_H + \mathrm{PIA}_H, \quad (3)$$

where PIA_H is the path-integrated attenuation at horizontal polarization (dB), r is the radar range (km), A_H is the specific attenuation at horizontal polarization (dB km^{-1}), γ is an empirical constant equal to 0.3006 in rain [average of γ values in Table 3 of Anagnostou et al. (2006)], and Z'_H is the corrected reflectivity at horizontal polarization. Another modification to the Anagnostou et al. (2006) technique was to relate the differential attenuation directly to PIA_H following Park et al. (2005) and Gorgucci et al. (2006). Once an initial estimate of PIA_H was made, the path-integrated differential attenuation PIA_{DP} was calculated as a function of PIA_H [Eq. (4)], and Z_{DR} was corrected with Eq. (5):

$$\mathrm{PIA}_{DP} = \varepsilon \times \mathrm{PIA}_H, \quad (4)$$

$$Z'_{DR} = Z_{DR} + \mathrm{PIA}_{DP}, \quad (5)$$

where Z'_{DR} is the corrected Z_{DR} and $\varepsilon = 0.173$ in rain.

2) Radar hydrometeor classification scheme

Once radar data were corrected for attenuation, the hydrometeor classification scheme from Snyder et al. (2010) was applied. This fuzzy logic scheme was originally devised at S band by Park et al. (2009) and adapted to X band by Snyder et al. (2010). The algorithm uses the following dual-polarization radar variables as inputs: Z_H, Z_{DR}, $10(\log K_{DP})$, copolar cross-correlation coefficient at lag zero (ρ_{HV}), reflectivity texture, and total differential phase texture. The membership functions used by the scheme are trapezoidal in shape and are derived from T-matrix simulations of observed and idealized PSDs of rain and hail. The membership functions are defined for six hydrometeor classes: ground clutter/anomalous propagation (GC/AP), biological scatterers (BS), big drops (BD), rain (RA), heavy rain (HR), and rain–hail mixture (RH). Only the latter four classes are retained for comparison with the PARSIVEL disdrometer, since the disdrometer does not detect GC/AP or BS. The output values of the membership functions are weighted according to Park et al. (2009) and then summed for each hydrometeor class. The class with the largest sum is then assigned to the radar range gate.

c. Radar–disdrometer comparison method

To select data for comparison, radar Z and Z_{DR} were averaged over a 3 × 3 array of range gates, centered on

the gate that contained the disdrometer. Time steps with sharp horizontal reflectivity gradients (>35 dB km^{-1}) and deployments with ground clutter ($Z > 0$ dBZ and near-zero Doppler velocity) near the disdrometer sites were excluded from the analysis. Radar and disdrometer data were then paired so that the time difference between the observations did not exceed 30 s.

Despite the exclusion of reflectivity gradients larger than 35 dB km^{-1} and the averaging of radar range gates, precipitation particle advection and the height difference between the radar beam and the surface are potentially large error sources in this analysis. As an example, consider a raindrop of $d = 1$ mm, which has a terminal fall speed of $v = 4$ m s^{-1}. If this drop is at a height of 1 km when the radar observes it, the drop will not reach the ground until 250 s later. Assuming a mean horizontal wind speed of 10 m s^{-1}, the drop will be advected 2.5 km downstream from the point in space where it was observed by the radar, a distance of nearly 34 radar range gates (in the worst case scenario). Thus, the PSDs observed by the radar and disdrometer may be different due to the strong low-level winds that often accompany supercell thunderstorms. A sensitivity test was performed in which the radar data were averaged over various windows, ranging from 3 × 3 to 11 × 11 range gates (not shown). Aside from a ~0.25-dB improvement in the Z_{DR} agreement when a 3 × 3 averaging window was used versus no averaging, the results are not affected by the size of the window. In addition, no correlation was found between the disagreement in the radar and disdrometer data and the radar beam height (not shown). Growth and evaporation of raindrops between the radar beam and the surface, however, are nevertheless error sources.

4. Results and discussion

a. Radar and disdrometer comparison of Z and Z_{DR}

1) X-BAND RADAR Z AND Z_{DR}

Figure 5 presents scatterplots of disdrometer and radar Z for all cases in the analysis (Table 1; Fig. 1) before (Fig. 5a) and after (Fig. 5b) the attenuation correction scheme was applied. Two data subsets are identified, which will be discussed in sections 4b and 4c: the 17 May 2010 hailstorm (red plus signs) and data with radar signal quality index (SQI) < 0.8 (blue plus signs). SQI (SIGMET 2009) is related to signal-to-noise ratio (SNR) and spectrum width (W):

$$\mathrm{SQI} = \frac{\mathrm{SNR}}{\mathrm{SNR}+1}\exp\left(-\frac{\pi^2 W^2}{2}\right). \qquad (6)$$

Of the 183 uncorrected radar Z values (97%), 177 are weaker than the corresponding disdrometer observations, with a median difference (radar Z − disdrometer Z) of −17 dB (all data in Fig. 5a). When the attenuation correction scheme is applied, the distribution shifts toward larger radar Z (all data in Fig. 5b). The median difference (radar Z − disdrometer Z) after attenuation correction is 1.0 dB, and 48% of the radar Z values are weaker than the disdrometer values. These statistics indicate that the attenuation correction scheme has removed the overall negative bias in the radar observations. Twenty-five percent of the radar Z values are larger than the PARSIVEL disdrometer sampling uncertainty, 30% are smaller, and 45% are within the sampling uncertainty (gray shading in Fig. 5), quantified by Jaffrain and Berne (2011). In the Jaffrain and Berne study, two PARSIVEL disdrometers were collocated and sampled ~990 h of light-to-moderate rainfall. The standard deviation of the difference in the moments (i.e., the sampling uncertainty) that were derived from each drop size distribution was then calculated (Tables B4 and B5 in Jaffrain and Berne 2011). Since the measurements in this study were taken in severe thunderstorms that often contained heavier rainfall rates, hail, and strong winds, the sampling uncertainty from Jaffrain and Berne (2011) should be considered a lower bound on the uncertainty in this research.

Scatterplots of Z_{DR} before and after attenuation correction are presented in Figs. 5c and 5d, respectively. Differential attenuation is clearly evident in the uncorrected radar Z_{DR}, with 50% of the radar observations having $Z_{DR} < 0$ dB (Fig. 5c). After attenuation correction was applied (Fig. 5d), the median difference (radar Z_{DR} − disdrometer Z_{DR}) improves from −2.7 to 0.19 dB. Of the corrected observations, 38% are within the sampling uncertainty of the PARSIVEL disdrometer (gray shaded region in Fig. 5d), compared to 20% prior to correction. Similar to the reflectivity, a large number of points lie outside the sampling uncertainty (gray shaded region in Fig. 5d), with 37% (25%) of the radar Z_{DR} values larger (smaller) than the disdrometer sampling uncertainty.

2) S-BAND RADAR Z

To provide a benchmark for comparison, disdrometer Z is also compared to Z from the nearest WSR-88D at the 0.5° elevation angle (Fig. 6) for all cases in the analysis. In comparing Fig. 5b to Fig. 6, we note that the median disagreement in radar and disdrometer Z is changed from 1.0 to −1.9 dB (all plus signs) when the S-band WSR-88D data are compared to the disdrometer-derived data. However, the median disagreement in Z for two of the data subsets (i.e., the 17 May 2010 hailstorm,

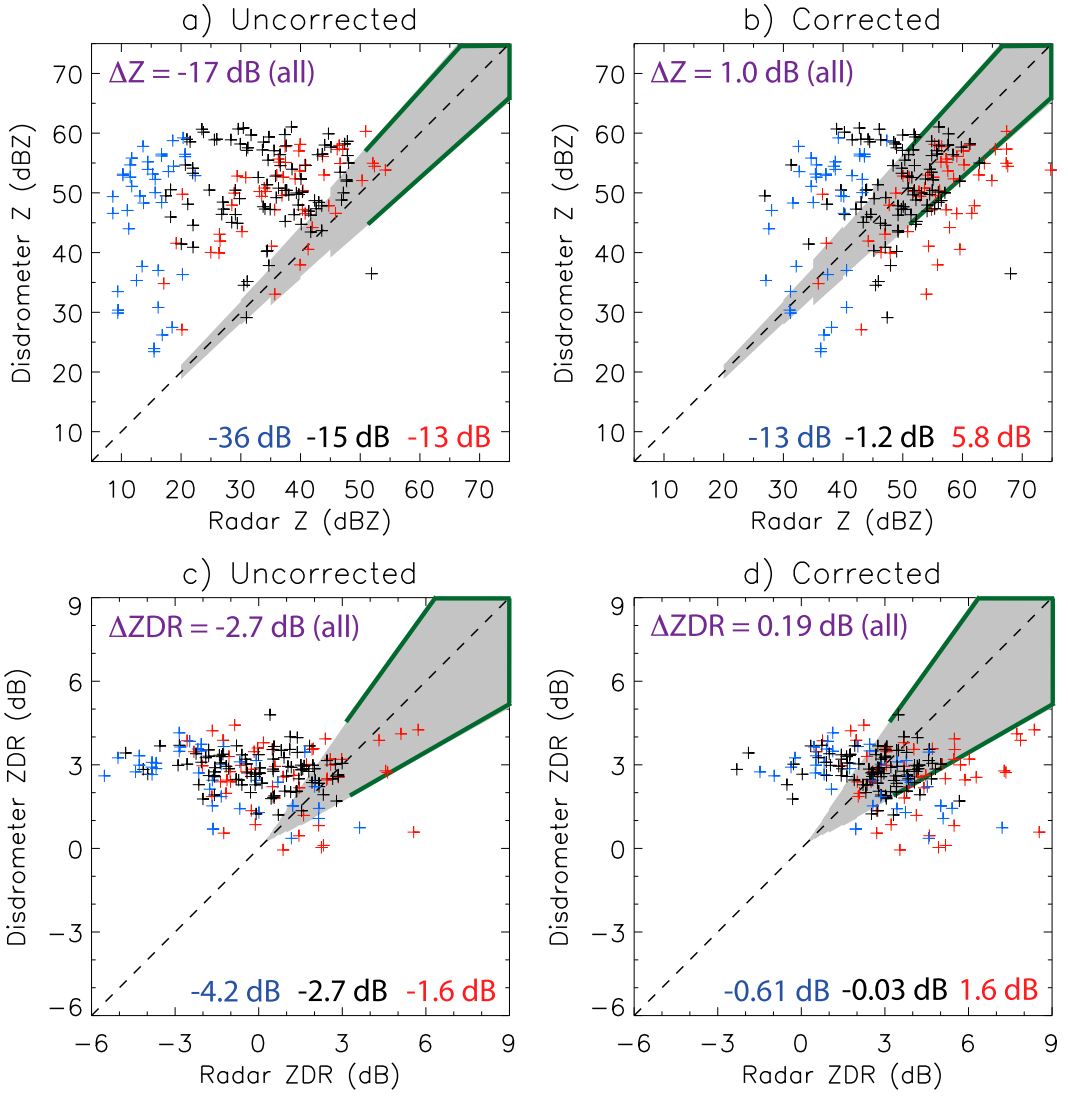

FIG. 5. Comparison of radar and disdrometer observations (left) before and (right) after attenuation correction for (a),(b) Z and (c),(d) Z_{DR}. The gray shaded region is the sampling uncertainty of the PARSIVEL disdrometer taken from Jaffrain and Berne (2011). Uncertainties for $Z > 50$ dBZ and $Z_{DR} > 3$ dB are outlined by the bold green lines and were obtained via linear extrapolation. Observations from the hailstorm on 17 May 2010 are plotted in red, while observations with radar SQI < 0.8 are plotted in blue. All other observations are plotted in black. Note that 4 of the 51 observations from the hailstorm have SQI < 0.8 and are included in the hailstorm subset. The median disagreement (radar − disdrometer) for all data is shown in the upper left, while the bottom right shows the median disagreement for each subset. The number of observations in each plot is 183, consisting of cases described in section 2a and Table 1.

red plus signs, and SQI < 0.8, blue plus signs) decreases when WSR-88D data are used, from 5.8 to −1.5 dB (hailstorm; red plus signs) and −13 to −0.66 dB (SQI $<$ 0.8; blue plus signs). These results imply that the X-band radar attenuation correction scheme partially contributes to the disagreement in these subsets, since S-band radar data compare more favorably with the disdrometer data (this inference, however, is complicated by differences in the X- and S-band radar beam heights; see Table 1). These details will be explored further in sections 4b–d, in which three case studies are examined: a supercell with large hail on 17 May 2010, a supercell on 9 June 2010, and a squall line on 12 June 2010.

b. *17 May 2010: Supercell with radar Z and Z_{DR} larger than disdrometer values*

On 17 May 2010, a high precipitation supercell thunderstorm was observed near Artesia, New Mexico.

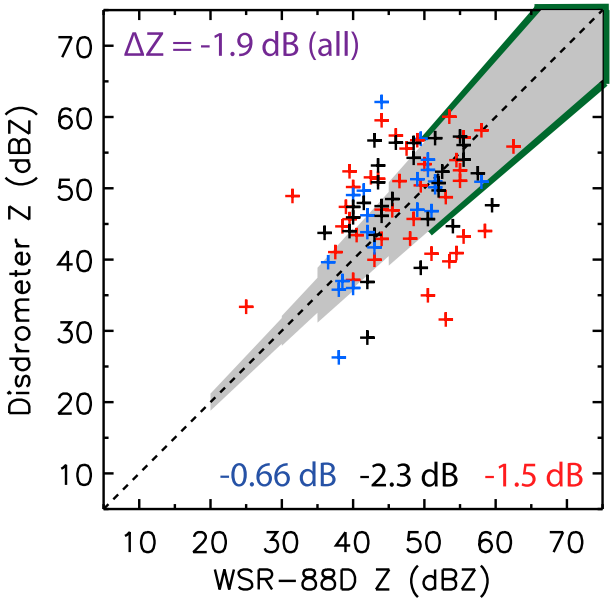

FIG. 6. As in Fig. 5b, but for unattenuated S-band WSR-88D Z.

The disdrometers sampled the forward-flank downdraft of the storm (Fig. 1a). The authors observed large hail ($d \sim 50$ mm) between 2220 and 2232 UTC, which severely damaged the windshields of the deployment vehicles. Figure 7 shows a time series plot comparing Z (Fig. 7a) and Z_{DR} (Fig. 7b) values recorded by the radar and disdrometer CU01 during this event. The total ice volume (assuming spherical particles) and the largest hail size observed by the disdrometer are also plotted with time (Figs. 7c,d). One might expect that the radar observations would not be heavily attenuated in the portion of the storm nearest the radar and that the attenuation could be accurately corrected. However, the time series data (Figs. 7a,b) reveal that, on average, corrected Z and Z_{DR} measured by the X-band radar were 8.3 and 1.5 dB larger, respectively, than the corresponding measurements from CU01. In fact, during the 27-min period shown, Z recorded by CU01 never exceeded that of the radar, and the CU01 Z_{DR} was greater than the radar Z_{DR} for only 2 of the 10 time steps. The trend of generally larger attenuation-corrected radar variables relative to all of the disdrometer measurements made on 17 May is also shown in Figs. 5b and 5d (red plus signs), a discrepancy that is not reflected in the remainder of the dataset (blue and black plus signs).

We hypothesize that the disagreement evident in the disdrometer and radar observations on 17 May is partly due to large, wet hail causing resonant (Mie) scattering of the radar beam. Because of Mie scattering, strong attenuation at horizontal polarization and differential attenuation have been observed at C- and X-bands in the presence of hail (e.g., Steiner et al. 2009; Tabary et al. 2009; Snyder et al. 2010; Borowska et al. 2011). Attenuation correction in the presence of hail is uncertain (Vulpiani et al. 2008; Borowska et al. 2011; Gu et al. 2011) because the relationship between differential phase and attenuation in a rain/hail mixture has only recently been examined. Ryzhkov et al. (2013a,b) found that the coefficients γ and ε in Eqs. (2) and (4) differ for rain and melting hail. Therefore, correcting attenuation in mixed-phase precipitation with coefficients meant for rain may lead to large errors (Steiner et al. 2009).

Because it is known that attenuation correction schemes designed for rain may perform poorly in the presence of hail, disdrometers can be used to detect hail on the ground and to flag radar observations beyond the location of the disdrometers as poor quality. Figure 8 shows the disdrometer data accumulated over this event as a function of particle fall velocity and diameter, with large hail up to $d = 20$ mm present (note that the measurement limit of the PARSIVEL disdrometer is $d = 26$ mm, and undercatchment is likely at these large sizes, as discussed later). Figure 7c shows that between 2218 and 2233 UTC, up to 15 cm^3 of ice were observed per 1-min time step by CU01. Although the ice volume decreases to $<5\ cm^3\ min^{-1}$ after 2233 UTC, a 5–15-dBZ discrepancy remains in Z, likely because the hail core is located between the radar and disdrometer sites. Range gates located behind the hail core may exhibit erroneous Z values due to the cumulative nature of attenuation correction errors.

An important limitation of this analysis is that large hail is sparse (number concentration of $10^{-2}\ m^{-3}$; Straka 2009) relative to the sample area (54 cm^2) of the PARSIVEL disdrometer. Therefore, disdrometer data might not indicate that radar data are suspect if only a few hailstones fall at the disdrometer site. In addition, even in thunderstorms with large amounts of ice, the PARSIVEL disdrometer will underestimate the hailstone concentration due to the small sample area. Undercatchment is especially likely for the largest hailstones, as Fig. 7d demonstrates that the largest hailstones detected by disdrometer CU01 during matched observations with the radar are $d = 13$ mm, despite hailstones of $d = 50$ mm being observed. In an attempt to determine whether undercatchment is the primary cause of the disagreement (rather than deficiencies in the attenuation correction scheme), we compare disdrometer Z to that of KFDX, the nearest S-band WSR-88D, at 0.5° elevation angle (Fig. 6). For the hailstorm case (red plus signs in Fig. 6), the median disagreement is −1.5 dB when S-band radar is used, but jumps to 5.8 dB for attenuation-corrected X-band radar (Fig. 5b). Note,

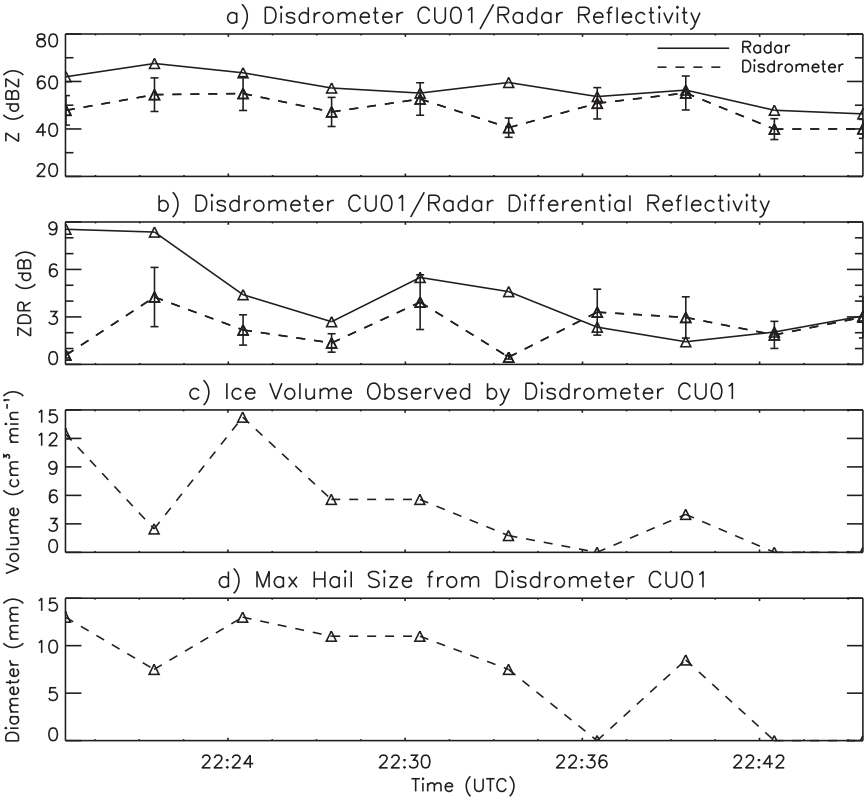

FIG. 7. Time series data recorded by NOXP (solid lines) and disdrometer CU01 (dashed lines) from the supercell thunderstorm with large hail ($d \sim 50$ mm) observed on 17 May 2010: (a) attenuation-corrected radar and disdrometer reflectivity, (b) attenuation-corrected radar and disdrometer differential reflectivity, (c) disdrometer-observed ice volume, and (d) disdrometer-observed maximum hail size. The error bars in (a),(b) represent the sampling uncertainty of the PARSIVEL disdrometer.

however, that the two radars are sampling at different heights (NOXP at 0.6 km AGL and KFDX at 4.2 km AGL; Table 1), which prevents us from making a definitive conclusion about the cause of the improved agreement.

c. *9 June 2010: Supercell thunderstorm with radar Z and Z_{DR} less than disdrometer values*

A supercell thunderstorm developed in the late afternoon of 9 June 2010 and moved into the western Nebraska panhandle near Scottsbluff. The core of the thunderstorm passed ~5 km south of the disdrometer deployments, which placed the disdrometers behind the precipitation core relative to the NOXP radar, which was deployed south of the storm core (Fig. 9a). Because the heaviest precipitation passed between the radar and disdrometers, the radar data collected near the disdrometer locations were heavily attenuated. Time series of corrected radar and disdrometer (UF01) data are shown in Figs. 10a and 10b. The radar SQI [Eq. (6)] is also plotted (Figs. 9b, 10c).

Between 0130 and 0140 UTC, the disdrometer recorded Z and Z_{DR} values that are 10–15 dB and 1–3 dB larger, respectively, than the values obtained by the radar after attenuation correction. During this time, SQI ranges from 0.4 to 0.5, which is poor relative to the other observations considered in this analysis (76% have SQI > 0.8). Data with SQI < 0.8 are plotted in blue in Fig. 5 and exhibit smaller radar Z relative to the disdrometer, a trend that is not present in the other data subsets (black and red plus signs). We find that the median disagreement in Z (radar Z − disdrometer Z) for SQI < 0.8 is −12 dB, while the median disagreement in Z for SQI > 0.8 is 2.1 dB. These results indicate that it is much more likely for radar Z to be smaller than disdrometer Z when SQI is small and most of the radar signal has been lost due to attenuation. To verify that the disagreement is not solely due to errors in the disdrometer data, we note from Fig. 6 (blue plus signs) that the comparison improves markedly for S-band radar data (median disagreement of −0.66 versus −13 dB for X-band radar data corrected for attenuation). The radar beam heights

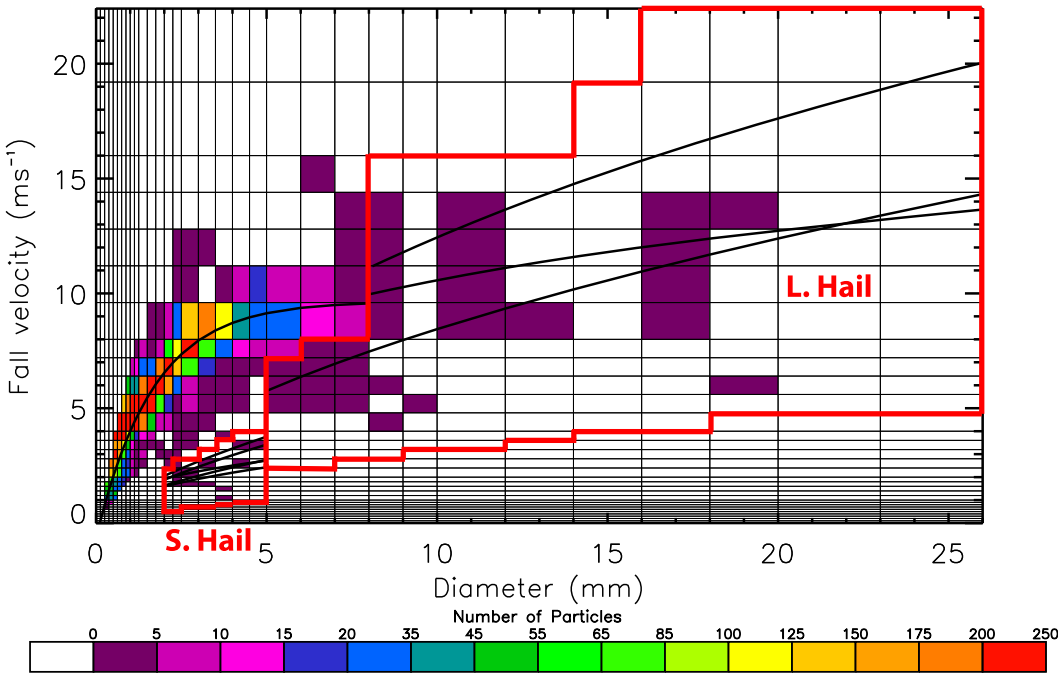

FIG. 8. Accumulated particle counts recorded by disdrometer CU01 on 17 May 2010 binned by the observed fall speed and diameter. The black lines represent the empirical fall speed–diameter relationships for rain, graupel, and hail that are shown in Fig. 4. Hail bins are outlined in red.

are also more similar than in the 17 May hailstorm (0.5 km AGL for NOXP and 1.5 km AGL for KCYS; Table 1). This evidence supports our claim that a negative bias exists in the attenuation-corrected NOXP radar data when SQI < 0.8.

d. *12 June 2010: Squall line with radar Z and Z_{DR} similar to disdrometer values*

At approximately 2100 UTC on 12 June 2010, a squall line developed near Gruver, Texas. Radar and disdrometer (UF05) time series data are shown in Fig. 11. The median attenuation-corrected radar and disdrometer Z and Z_{DR} values are in closer agreement than in previous case studies (5.0 and 1.2 dB, respectively). The best agreement (to within 5 and 0.5 dB) is found from 2139 to 2155 UTC, with greater disagreement (>15 and >1.5 dB) during the first two time steps (i.e., 2130 and 2136 UTC). From 2130 to 2136 UTC, the radar data (Fig. 12) show that a small convective cell (~2 km in north-to-south extent) near the leading edge of the squall line moves over disdrometer UF05. The ice volume recorded by the disdrometer (Fig. 11c) is largest during this time period, peaking at 5.6 $cm^3 min^{-1}$ at 2130 UTC, before dropping below 4 $cm^3 min^{-1}$ after 2139 UTC. The time series of maximum hail size (Fig. 11d) and accumulated PSD (Fig. 13) also depict the hail from the convective cell and show hailstones up to $d = 13$ mm. From 2130 to 2136 UTC, hail resulted in larger radar Z and Z_{DR} values relative to the disdrometer data (Fig. 11), which is the same result found in section 4b. A radial stripe of suspiciously large radar Z (>55 dBZ) and Z_{DR} (>6 dB) values is also present in the radar imagery at 2136 UTC (red circles in Fig. 12) in the southwestern portion of the squall line, possibly caused by the presence of hail there.

Following the passage of the convective cell and the hail at ~2137 UTC at the disdrometer site, agreement in Z and Z_{DR} improves and the discrepancies are generally within 5 and 0.5 dB, respectively. During the period of agreement (2137–2155 UTC), the radar imagery depicts precipitation that is nearly uniform in time and space near the disdrometer site. Additionally, the observed ice volume remains small (median 0.7 $cm^3 min^{-1}$), suggesting that hail is not biasing the attenuation correction. The large radar SQI (>0.95, not shown) and the relative absence of hail are the likely reasons for the improved agreement.

e. *Radar and disdrometer hydrometeor classification comparisons*

We now compare output from the radar and disdrometer hydrometeor classification schemes. All of the disdrometer and radar data from Fig. 5 are included. The disdrometer hydrometeor classes consist of rain (RA),

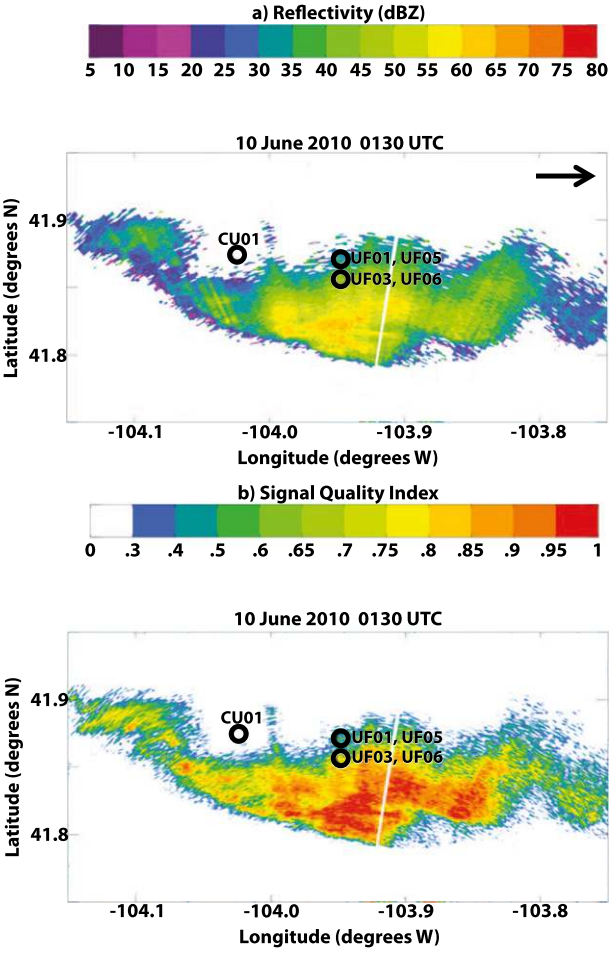

FIG. 9. Plan position indicator observations of (a) attenuation-corrected radar reflectivity and (b) SQI for the supercell thunderstorm observed by NOXP at 1° elevation angle at 0130 UTC 10 Jun 2010. Black open circles denote disdrometer locations. The arrow shows the direction of storm motion. The distance between each labeled tick mark is approximately 8 km in X and 11 km in Y.

small hail (S. Hail), and large hail (L. Hail), while the radar classes of interest are BD, RA, HR, and RH. Because the radar scheme does not have firm rain rate or reflectivity thresholds that can be applied to the disdrometer data to discriminate between BD, RA, and HR, these radar classes are combined into a general rain class. Therefore, the purpose of the comparison is to analyze the agreement between the liquid and ice classes of the two schemes. Because of error sources that include overlapping rain and hail signatures in the radar data, errors in attenuation and differential attenuation correction, and particle advection, we do not expect perfect agreement; however, we can nevertheless use the data to explain under what conditions we expect disagreement and why.

The comparison results are shown in Fig. 14. Sectors that represent disagreement [i.e., the disdrometer (radar) observes hail, but the radar (disdrometer) does not] are separated from the remainder of the chart. Of the 179 observations, 113 (63%) are in agreement. The most common scenarios are that both schemes detect hail (36% of the time) or that both detect rain (27% of the time). Of the 60 observations that disagree, 13 (7%) of them disagree because the radar scheme identifies hail when the disdrometer does not observe any. One likely explanation for this disagreement is that due to the sparseness of the hail, no hailstones passed through the sample volume of the disdrometer during the same time step as observed by the radar. In addition, it is also possible that the hail melted as it fell from the height of the radar volume to the disdrometer. Since the center of the radar beam was always 0.2–1 km AGL for the observations considered here, this possibility is most likely when small hail was present at the height of the radar beam, which would be more susceptible to complete melting.

Disagreement in the remaining 53 observations (29%) results from the disdrometer detecting hail when the radar does not. It is important to note that the disdrometer ice scheme does not account for the number of hailstones present; if just one hailstone is recorded during a 60-s time step, a classification of hail is still assigned by the disdrometer scheme, even though hail may not be the dominant contributor to the corresponding radar measurements. The median number of hailstones and median hailstone size observed in a 60-s time step by the disdrometer is greater when both the radar and the disdrometer schemes agree that hail is present (median of two hailstones and 8.5 mm when the schemes agree versus one hailstone and 6.0 mm). The radar classification scheme uses the dual-polarization radar variables to identify the dominant hydrometeor class within the radar volume, but other hydrometeor types may nevertheless be present. Thus, it may be that the radar scheme does not assign the hail class when the radar volume is dominated by rain and there are relatively few small hailstones present. This is possible because the membership functions for rain and hail in the radar fuzzy logic scheme overlap, but it is only the class with the maximum rule strength (i.e., the maximum weighted sum of the membership function values) that is assigned to the radar range gate. When the disdrometer classifies hail but the radar does not, the median rule strength of the radar hail (rain) class is 0.6 (1.5), compared to 0.5 (1.5) when both instruments classify rain. However, the radar algorithm will not classify hail in either case because rain is the dominant scatterer in the radar volume.

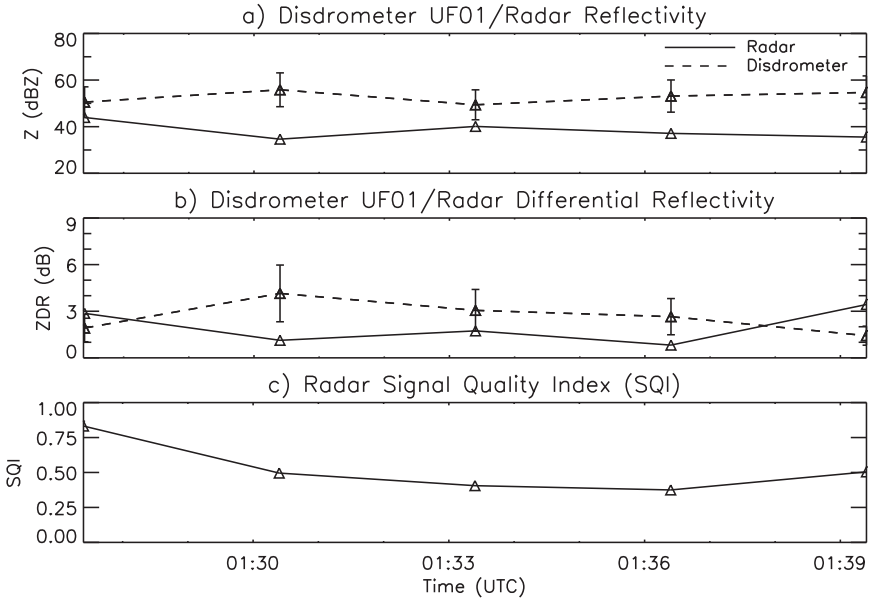

FIG. 10. As in Fig. 7, but for the supercell thunderstorm observed by disdrometer UF01 on 9 Jun 2010. The radar SQI is shown in (c).

An additional factor that is likely to cause the PARSIVEL disdrometer to report hail when the radar does not is the possibility that multiple particles may be present within the disdrometer sample volume at the same time. If two 5-mm raindrops were present in the sample volume, for instance, the disdrometer would record a single 10-mm particle, which would be classified as a hailstone (Fig. 4). For a simulated

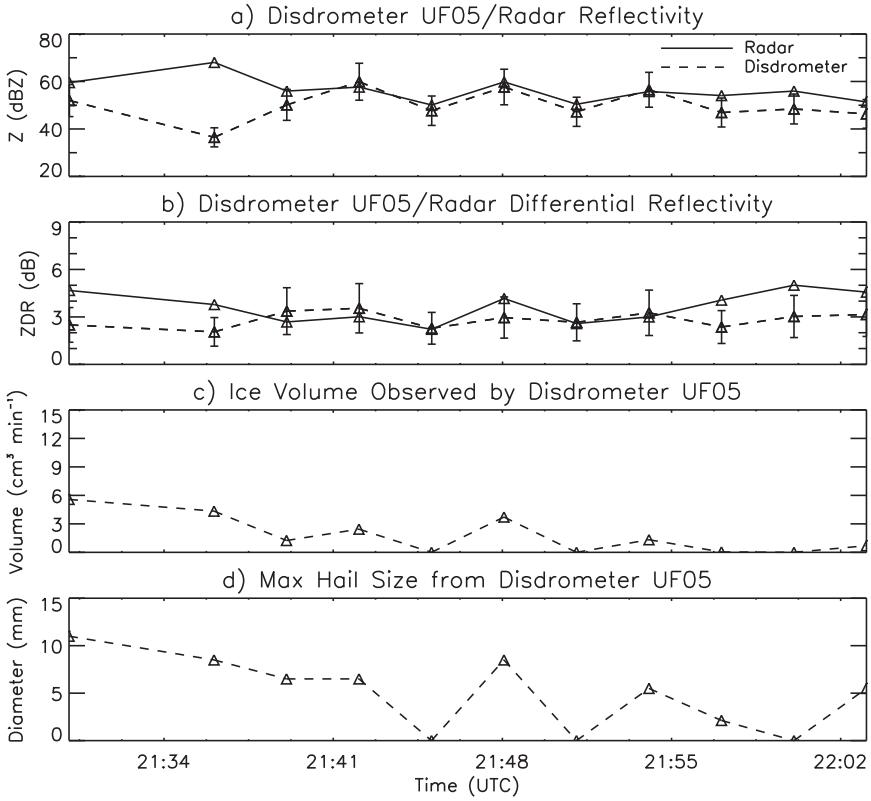

FIG. 11. As in Fig. 7, but for the squall line observed by disdrometer UF05 on 12 Jun 2010.

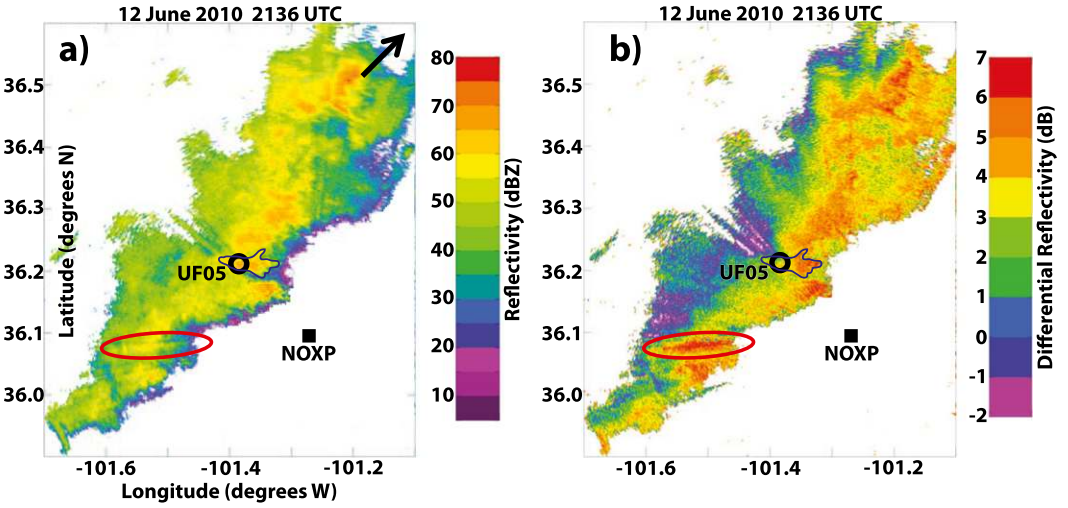

FIG. 12. Plan position indicator observations of attenuation-corrected (a) radar reflectivity and (b) differential reflectivity for the squall line observed by NOXP at 1° elevation angle at 2136 UTC 12 Jun 2010. The location of disdrometer UF05 is denoted by the black open circle and the location of NOXP is annotated. The convective cell is outlined in blue, and an area of large radar reflectivity and differential reflectivity is circled in red. The arrow in (a) indicates the storm motion direction. The distance between each labeled tick mark is approximately 18 km in X and 11 km in Y.

heavy convective rain with intercept parameter $N_0 = 1400\,\mathrm{m}^{-3}\,\mathrm{mm}^{-1}$ and rainfall rate $R = 300\,\mathrm{mm\,h}^{-1}$, Löffler-Mang and Joss (2000) found that the probability of coincidences in the PARSIVEL disdrometer sample volume is ~5%. Therefore, disagreement between the hail detections of the radar and disdrometer schemes is possible due to a combination of particle coincidences in the disdrometer sample volume and the use of the fuzzy logic scheme for classifying the radar data.

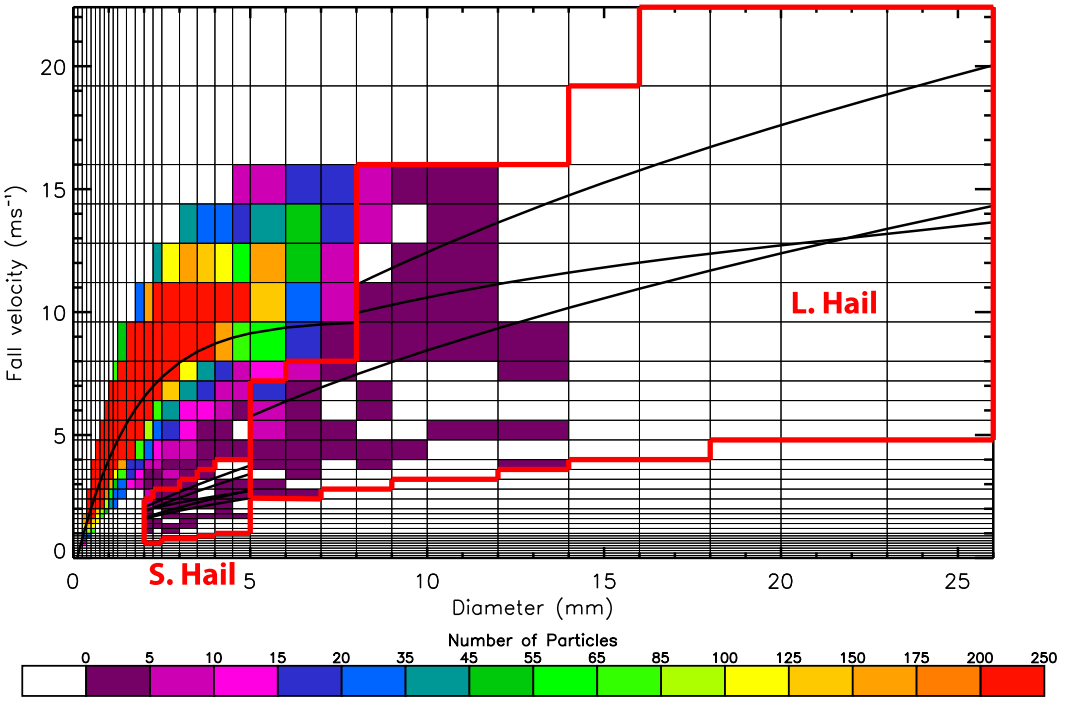

FIG. 13. As in Fig. 8, but for disdrometer UF05 on 12 Jun 2010.

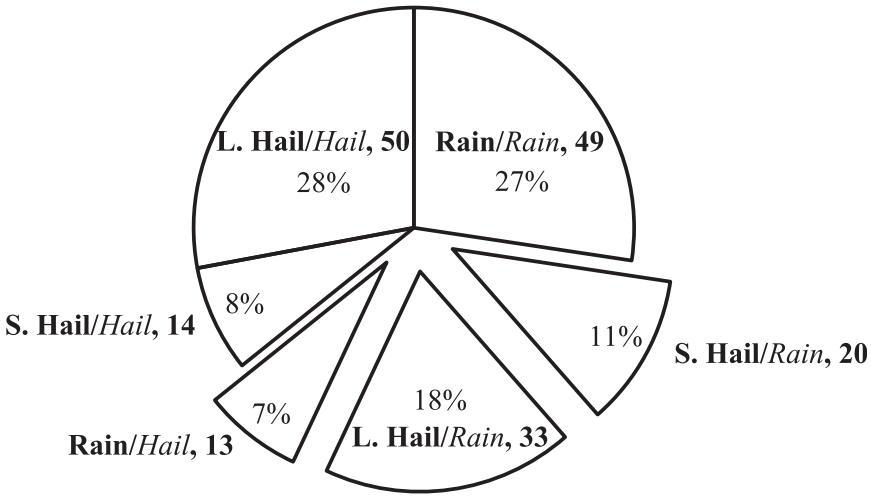

FIG. 14. Pie chart comparing the outputs from the disdrometer and radar hydrometeor classification schemes. The area of each sector in the pie chart is proportional to the percentage of the total number of time steps (179) included in each sector. Each sector is labeled with the class assigned by the disdrometer scheme (i.e., rain, small hail, and large hail) in bold, followed by a solidus (/) and the class assigned by the radar scheme (i.e., rain and hail) in italics. The number of time steps in each sector is also listed. Sectors in which the outputs from the two schemes disagree have been separated from the rest of the chart.

5. Summary and conclusions

In this paper, we applied an attenuation correction scheme designed for rain (Steiner et al. 2009) to X-band dual-polarization radar data collected by NOXP in five supercell thunderstorms and one squall line during the VORTEX2 field campaign in 2010. The attenuation-corrected radar Z and Z_{DR} were then compared to those derived from PSDs recorded by PARSIVEL disdrometers using the T-matrix program, which required assumptions to be made about the axis ratio, fractional water content, and canting angle of the observed hailstones (see Table 3 and appendix A). The Snyder et al. (2010) hydrometeor classification scheme was then applied to the corrected radar data, and the results were compared to the output from a hydrometeor classification scheme that was developed for disdrometers in convective weather.

When the disdrometer and attenuation-corrected radar data were compared, it was shown that 45% (38%) of the Z (Z_{DR}) observations agree to within the sampling uncertainty of the PARSIVEL disdrometer (Figs. 5b,d). A case study analysis of a supercell thunderstorm with large hail demonstrated that the attenuation-corrected X-band radar Z (Z_{DR}) tends to be larger than the values recorded by the disdrometer by 8.3 dB (1.5 dB), respectively (Fig. 7a). However, when S-band WSR-88D and disdrometer Z are compared, the measurements differ by only −1.5 dB (red plus signs in Fig. 6). The discrepancy between the X-band radar data and the disdrometer measurements is possibly due to the attenuation correction scheme overcorrecting the radar data within and behind the hail core of the supercell thunderstorm, although undercatchment of large hailstones by the disdrometer may have also contributed to the disagreement. A second case study of a supercell thunderstorm (Fig. 10) demonstrated that the disdrometer tends to record larger Z and Z_{DR} (by 13 and 0.61 dB, respectively) than the X-band radar when the radar signal quality is poor (SQI $<$ 0.8). For the same data subset, only a 0.66-dB discrepancy in Z exists when the disdrometer and WSR-88D are compared (blue plus signs in Fig. 6). Disagreement between the disdrometer and attenuation-corrected X-band radar data due to poor SQI is most likely to occur within trailing precipitation that is located behind heavy rainfall (relative to the radar location). A third case study analysis showed that when 1) large hail is not detected, 2) the radar signal quality is good (SQI $>$ 0.8), and 3) the precipitation structure is horizontally homogeneous, Z and Z_{DR} observations from both instruments agree to within 5 and 0.5 dB (2137–2155 UTC in Fig. 11).

When the hydrometeor classification schemes for the radar and the disdrometer are compared (Fig. 14), they agree 63% of the time. Disagreement results when the radar scheme diagnoses hail and the disdrometer scheme does not (7% of the observations) and when the disdrometer observes hail and it is not detected by

the radar scheme (29%). Hail may be detected solely by the radar because small hail is present in the radar volume that melts prior to reaching the surface or because the hail was especially sparse and not detected by the disdrometer. When the opposite situation occurred (i.e., the disdrometer observed hail but the radar scheme did not), it was shown that fewer, smaller hailstones were observed by the disdrometer than when the two instruments both observed hail. In these cases, the nonzero rule strength (i.e., the weighted sum of the membership function values) of the hail class suggests that hail may have been present in the radar volume, but because the radar hydrometeor classification scheme identifies the most dominant hydrometeor in the sampling volume, the hail was not classified.

The data quality analysis presented here may be particularly valuable to those who undertake future VORTEX2 microphysical process and data assimilation studies. We have shown that attenuation of radar data in severe thunderstorms can be substantial even in the portion of the thunderstorm that is initially penetrated by the radar beam. Further, since the assumptions in the attenuation correction scheme used in this study are not valid in ice, large errors may result in and beyond hail cores. This research may also be helpful to those who use the VORTEX2 disdrometer observations to validate model-predicted surface precipitation types. With the hydrometeor classification scheme in Fig. 4, median diameter and number concentration can be derived from the disdrometer data for each hydrometeor class and compared to those from numerical models.

Acknowledgments. This research was sponsored by NSF ATM-0910424 and NSF DGE-1144083. Funding for Donald Burgess came from NOAA/Office of Oceanic and Atmospheric Research under NOAA–University of Oklahoma Cooperative Agreement NA11OAR430072. Funding for NOXP data came from NSF ATM-0802717. We thank Gwo-Jong Huang and Prof. Bringi (Colorado State University) for the T-matrix program, in addition to George Fernandez, Carlos Lopez, and Forrest Masters (University of Florida), who designed the articulating disdrometers and supplied four of the stationary disdrometers. We also thank Stephanie Higgins (University of Colorado) for writing many of the routines that process the disdrometer data. We are grateful to George Fernandez, Stephanie Higgins, Rachel Humphrey, Scott Landolt, Carlos Lopez, Daniel Nuding, and Cameron Redwine for deploying instruments during VORTEX2. The helpful feedback from two anonymous reviewers substantially improved an earlier version of this manuscript. Any opinions, findings, or recommendations expressed in this publication are those of the authors and do not necessarily reflect the views of the National Science Foundation.

APPENDIX A

Sensitivity to Hailstone Characteristics in the T-Matrix Program

To calculate Z and Z_{DR} from disdrometer data that contain hail, characteristics of the hail must be specified, including axis ratio, fractional water content, and fall behavior. Table 3 provides the default values used in this analysis. However, since no measurements of axis ratio, fractional water content, or canting angle were made, the chosen values represent a source of uncertainty. Here, we examine the sensitivity of the results to some of the hailstone characteristics in the T-matrix scattering calculations.

To quantify the sensitivity, we select the PSD observed by disdrometer CU01 on 17 May 2010 (Fig. 8), since these data are from a hailstorm and should exhibit the greatest sensitivity to the hailstone characteristics. The quantities Z and Z_{DR} are calculated for two values of the fractional water content of small hail (0.35 and 0.65), axis ratio of large hail (0.5 and 0.65), and canting angle standard deviation of all hail (35° and 65°). These values, together with those provided in Table 3, provide a reasonable range over which these characteristics can be expected to vary (Knight 1986; Lesins and List 1986; Ryzhkov et al. 2011). The resulting sensitivities in Z and Z_{DR} for the entire time series recorded by CU01 are shown in Fig. A1, relative to Z and Z_{DR} obtained using the default values of the parameters in Table 3. No sensitivity is evident with respect to the small hail fractional water content (Fig. A1a). In contrast, up to 2-dB sensitivity in Z and 0.9 dB in Z_{DR} is present when the large hail axis ratio is varied (Fig. A1b), although these sensitivities are only present in ~5 time steps of the disdrometer data. The Z and Z_{DR} display more consistent sensitivity to hail canting angle standard deviation, although this sensitivity remains within 0.2 and 0.6 dB, respectively (Fig. A1c). Considering only the data included in Fig. 5 from CU01 on 17 May (Table A1), the mean sensitivity in Z (Z_{DR}) to large hail axis ratio and hail canting angle standard deviation, respectively, is just −0.01 dB (0.03 dB) and 0.05 dB (0.1 dB). Similar results (Table A1) were obtained from the PSD observed by disdrometer UF05 on 12 June 2010 (Fig. 13).

In summary, because the PSDs in this study contain little hail relative to rain, Z and Z_{DR} exhibit limited sensitivity to the hailstone axis ratio, fractional water

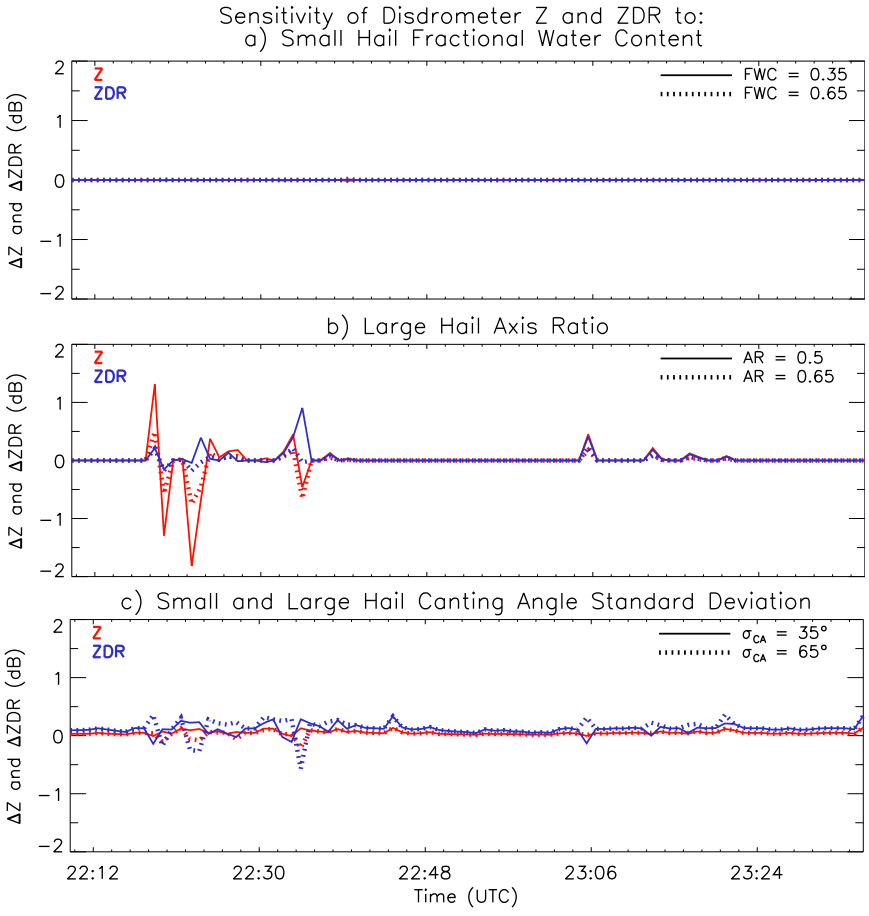

FIG. A1. Sensitivity of Z (red lines) and Z_{DR} (blue lines) from disdrometer CU01 on 17 May 2010 to (a) fractional water content of small hail, (b) axis ratio of large hail, and (c) canting angle standard deviation of small and large hail. The sensitivities are relative to the Z and Z_{DR} obtained by using the default values of small hail fractional water content (0.5), large hail axis ratio (0.8), and small and large hail canting angle standard deviation (50°).

content, and canting angle. This result does not mean that Z and Z_{DR} are *generally* insensitive to hailstone characteristics. Rather, the small sample volume of the PARSIVEL disdrometer caused relatively few hailstones to be observed, which reduced the sensitivity of the results to the hailstone characteristics and meant that rain was the dominant contributor to Z and Z_{DR}.

APPENDIX B

Sensitivity to Disdrometer Hydrometeor Classification Scheme

A partially melted hailstone of a given diameter can exhibit a range of fall speeds depending on its fractional water content and bulk density (Rasmussen and Heymsfield 1987). In the disdrometer hydrometeor classification scheme of Friedrich et al. (2013b), fall speed curves for dry graupel (Locatelli and Hobbs 1974) are used to determine the fall speed thresholds for the small hail region with $2 < d < 5$ mm (Fig. 4). Because small hailstones in supercell thunderstorms have a bulk density greater than that of graupel and are likely embedded in a torus of liquid water, it is reasonable to expect that these particle fall speeds are greater than the graupel curves offered by Locatelli and Hobbs (1974), but somewhat less than the fall speeds for pure rain given by Atlas et al. (1973). In the Friedrich et al. (2013b) classification scheme, such particles are left unclassified (see Fig. 4) and are excluded from T-matrix computations of Z and Z_{DR}, since there is uncertainty about whether they should be modeled as rain or small hail.

TABLE A1. Mean sensitivity in disdrometer Z and Z_{DR} to small hail FWC, axis ratio (AR) of large hail, small and large hail canting angle standard deviation (σ_{CA}), and the disdrometer hydrometeor classification scheme for two subsets of the data in Fig. 5: observations from disdrometer CU01 on 17 May 2010 and observations from disdrometer UF05 on 12 Jun 2010. All values are relative to those obtained using the default parameters listed in Table 3 and the disdrometer hydrometeor classification scheme shown in Fig. 4.

Sensitivity test	17 May 2010 (CU01) ΔZ (dB) ΔZ_{DR} (dB)	12 Jun 2010 (UF05) ΔZ (dB) ΔZ_{DR} (dB)
FWC = 0.65	0.000 471	0.001 77
	−0.000 195	−0.000 917
FWC = 0.35	−0.000 391	−0.001 36
	0.000 138	0.000 702
AR = 0.65	−0.0110	0.0152
	0.009 54	0.0114
AR = 0.5	−0.004 70	0.0399
	0.0340	0.0110
σ_{CA} = 35°	0.0412	0.0669
	0.130	0.190
σ_{CA} = 65°	0.0507	0.0687
	0.116	0.141
Unclassified particles	0.193	0.0401
are rain	0.0116	−0.001 68
Unclassified particles	0.121	0.0105
are small hail	−0.0133	−0.006 87
Small hail particles	−0.004 43	−0.0158
removed	0.001 94	0.0103

To examine the sensitivity of Z and Z_{DR} to these excluded particles, we again use the data recorded by disdrometer CU01 during the 17 May 2010 hailstorm (Fig. 8) and compute Z and Z_{DR} for two different tests: one that assumes the previously unclassified particles are rain, and a second that assumes the particles are hail. Figure B1a illustrates the sensitivity in Z (red lines) and Z_{DR} (blue lines) for both the rain (solid lines) and hail (broken lines) tests. Up to 13-dB (1.5 dB) sensitivity in Z (Z_{DR}) is evident for the time step at 2212 UTC. However, in all but one of the other 86 1-min time steps, negligible sensitivity is present. The reason for the large sensitivity at 2212 UTC is due to small disdrometer reflectivity (23 dBZ, not shown), coupled with a relatively large particle of d = 4.25 mm within the unclassified region. Because of the small total number of particles observed at 2212 UTC, the particle within the unclassified region has marked influence on Z and Z_{DR}. In heavy rainfall typical of the thunderstorms observed in this study, however, Z and Z_{DR} are relatively insensitive to whether particles in the unclassified region are discounted or assumed to be rain or hail. Table A1 indicates that for the data included in Fig. 5 from CU01 on 17 May, the mean sensitivity to the unclassified region is less than 0.2 and 0.02 dB for Z and Z_{DR}, respectively. In fact, when all small hail particles are removed from the 17 May PSD, Fig. B1b shows that Z and Z_{DR} change by less than 0.2 dB for the entire time series recorded by CU01. For the data included in Fig. 5, the mean change in Z (Z_{DR}) is −0.004 dB (0.002 dB; see Table A1). These tests demonstrate that despite the uncertainty in small hailstone characteristics, the impact on the results is small, likely because the PSDs examined here contain little small hail compared to rain.

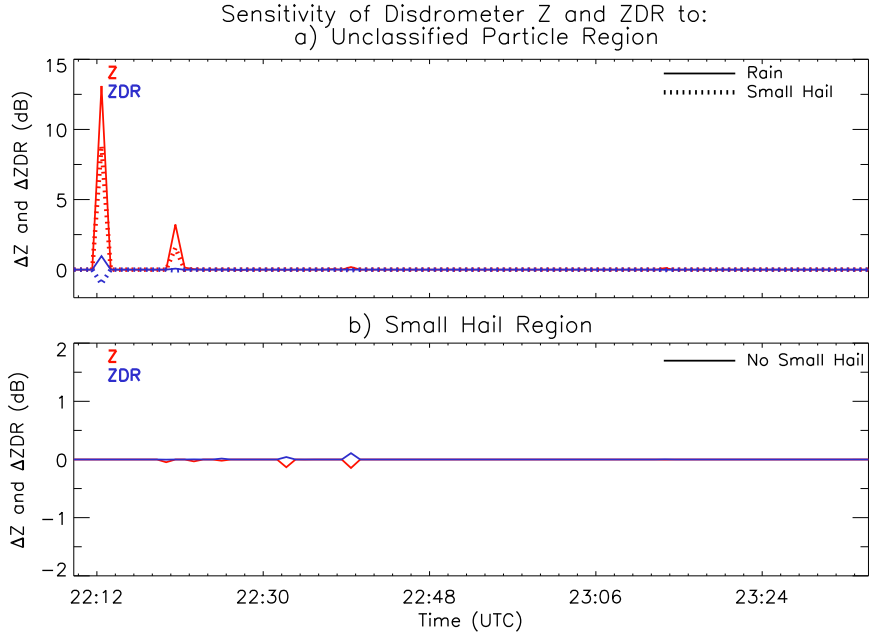

FIG. B1. As in Fig. A1, but for (a) the precipitation type of the particles in the unclassified region in Fig. 4 and (b) the small hail region in Fig. 4. The sensitivities are relative to the Z and Z_{DR} obtained by (a) excluding the unclassified particles and (b) including the small hail particles.

REFERENCES

Anagnostou, M. N., E. N. Anagnostou, and J. Vivekanandan, 2006: Correction for rain path specific and differential attenuation of X-band dual-polarization observations. *IEEE Geosci. Remote Sens.,* **44,** 2470–2480, doi:10.1109/TGRS.2006.873204.

Atlas, D., R. C. Srivastava, and R. S. Sekhon, 1973: Doppler radar characteristics of precipitation at vertical incidence. *Rev. Geophys. Space Phys.,* **11,** 1–35, doi:10.1029/RG011i001p00001.

Aydin, K., S. H. Park, and T. M. Walsh, 1998: Bistatic dual-polarization scattering from rain and hail at S- and C-band frequencies. *J. Atmos. Oceanic Technol.,* **15,** 1110–1121, doi:10.1175/1520-0426(1998)015<1110:BDPSFR>2.0.CO;2.

Balakrishnan, N., and D. S. Zrnić, 1990: Use of polarization to characterize precipitation and discriminate large hail. *J. Atmos. Sci.,* **47,** 1525–1540, doi:10.1175/1520-0469(1990)047<1525:UOPTCP>2.0.CO;2.

Barthazy, E., S. Göke, R. Schefold, and D. Högl, 2004: An optical array instrument for shape and fall velocity measurements of hydrometeors. *J. Atmos. Oceanic Technol.,* **21,** 1400–1416, doi:10.1175/1520-0426(2004)021<1400:AOAIFS>2.0.CO;2.

Beard, K. V., and C. H. Chuang, 1987: A new model for the equilibrium shape of raindrops. *J. Atmos. Sci.,* **44,** 1509–1524, doi:10.1175/1520-0469(1987)044<1509:ANMFTE>2.0.CO;2.

Borowska, L., A. Ryzhkov, D. Zrnić, C. Simmer, and R. Palmer, 2011: Attenuation and differential attenuation of 5-cm-wavelength radiation in melting hail. *J. Appl. Meteor. Climatol.,* **50,** 59–76, doi:10.1175/2010JAMC2465.1.

Bringi, V. N., and V. Chandrasekar, 2001: *Polarimetric Doppler Weather Radar: Principles and Applications.* Cambridge University Press, 662 pp.

——, T. D. Keenan, and V. Chandrasekar, 2001: Correcting C-band radar reflectivity and differential reflectivity data for rain attenuation: A self-consistent method with constraints. *IEEE Trans. Geosci. Remote Sens.,* **39,** 1906–1915, doi:10.1109/36.951081.

——, V. Chandrasekar, J. Hubbert, E. Gorgucci, W. L. Randeu, and M. Schoenhuber, 2003: Raindrop size distribution in different climatic regimes from disdrometer and dual-polarized radar analysis. *J. Atmos. Sci.,* **60,** 354–365, doi:10.1175/1520-0469(2003)060<0354:RSDIDC>2.0.CO;2.

Burgess, D. W., E. R. Mansell, C. M. Schwarz, and B. J. Allen, 2010: Tornado and tornadogenesis events seen by the NOXP X-band, dual-polarization radar during VORTEX2 2010. Preprints, *25th Conf. on Severe Local Storms,* Denver, CO, Amer. Meteor. Soc., 5.2. [Available online at http://ams.confex.com/ams/25SLS/techprogram/paper_176164.htm.]

Carey, L. D., S. A. Rutledge, D. A. Ahijevych, and T. D. Keenan, 2000: Correcting propagation effects in C-band polarimetric radar observations of tropical convection using differential propagation phase. *J. Appl. Meteor.,* **39,** 1405–1433, doi:10.1175/1520-0450(2000)039<1405:CPEICB>2.0.CO;2.

Dolan, B., and S. A. Rutledge, 2009: A theory-based hydrometeor identification algorithm for X-band polarimetric radars. *J. Oceanic Atmos. Technol.,* **26,** 2071–2088, doi:10.1175/2009JTECHA1208.1.

Friedrich, K., S. A. Higgins, F. J. Masters, and C. R. Lopez, 2013a: Articulating and stationary PARSIVEL disdrometer measurements in conditions with strong winds and heavy rainfall. *J. Atmos. Oceanic Technol.,* **30,** 2063–2080, doi:10.1175/JTECH-D-12-00254.1.

——, E. A. Kalina, F. J. Masters, and C. R. Lopez, 2013b: Drop-size distributions in thunderstorms measured by optical disdrometers during VORTEX2. *Mon. Wea. Rev.,* **141,** 1182–1203, doi:10.1175/MWR-D-12-00116.1.

Geotis, S. G., 1978: Comparison of reflectivity measurements by radar and by disdrometer. *J. Appl. Meteor.,* **17,** 1403–1405, doi:10.1175/1520-0450(1978)017<1403:CORMBR>2.0.CO;2.

Goddard, J. W. F., S. M. Cherry, and V. N. Bringi, 1982: Comparison of dual-polarization radar measurements of rain with ground-based disdrometer measurements. *J. Appl. Meteor.,* **21,** 252–256, doi:10.1175/1520-0450(1982)021<0252:CODPRM>2.0.CO;2.

Gorgucci, E., V. Chandrasekar, and L. Baldini, 2006: Correction of X-band radar observation for propagation effects based on the self-consistency principle. *J. Atmos. Oceanic Technol.,* **23,** 1668–1681, doi:10.1175/JTECH1950.1.

Grzych, M. L., B. D. Lee, and C. A. Finley, 2007: Thermodynamic analysis of supercell rear-flank downdrafts from Project ANSWERS. *Mon. Wea. Rev.,* **135,** 240–246, doi:10.1175/MWR3288.1.

Gu, J.-Y., A. Ryzhkov, P. Zhang, P. Neilley, M. Knight, B. Wolf, and D.-I. Lee, 2011: Polarimetric attenuation correction in heavy rain at C band. *J. Appl. Meteor. Climatol.,* **50,** 39–58, doi:10.1175/2010JAMC2258.1.

Gunn, R., and G. D. Kinzer, 1949: The terminal velocity of fall for water droplets in stagnant air. *J. Meteor.,* **6,** 243–248, doi:10.1175/1520-0469(1949)006<0243:TTVOFF>2.0.CO;2.

Huang, G. J., V. N. Bringi, S. van den Heever, and W. Cotton, 2005: Polarimetric radar signatures from RAMS microphysics. Preprints, *32nd Int. Conf. on Radar Meteorology,* Albuquerque, NM, Amer. Meteor. Soc., P11R.6. [Available online at http://ams.confex.com/ams/pdfpapers/96261.pdf.]

——, ——, and M. Thurai, 2008: Orientation angle distributions after an 80-m fall using a 2D video disdrometer. *J. Atmos. Oceanic Technol.,* **25,** 1717–1723, doi:10.1175/2008JTECHA1075.1.

——, ——, R. Cifelli, D. Hudak, and W. A. Petersen, 2010: A methodology to derive radar reflectivity–liquid equivalent snow rate relations using C-band radar and a 2D video disdrometer. *J. Atmos. Oceanic Technol.,* **27,** 637–651, doi:10.1175/2009JTECHA1284.1.

Hubbert, J., and V. N. Bringi, 1995: An iterative filtering technique for the analysis of coplanar differential phase and dual-frequency radar measurements. *J. Atmos. Oceanic Technol.,* **12,** 643–648, doi:10.1175/1520-0426(1995)012<0643:AIFTFT>2.0.CO;2.

——, S. M. Ellis, M. Dixon, and G. Meymaris, 2010a: Modeling, error analysis, and evaluation of dual-polarization variables obtained from simultaneous horizontal and vertical polarization transmit radar. Part I: Modeling and antenna errors. *J. Atmos. Oceanic Technol.,* **27,** 1583–1598, doi:10.1175/2010JTECHA1336.1.

——, ——, ——, and ——, 2010b: Modeling, error analysis, and evaluation of dual-polarization variables obtained from simultaneous horizontal and vertical polarization transmit radar. Part II: Experimental data. *J. Atmos. Oceanic Technol.,* **27,** 1599–1607, doi:10.1175/2010JTECHA1337.1.

Illingworth, A. J., and C. J. Stevens, 1987: An optical disdrometer for the measurement of raindrop size spectra in windy conditions. *J. Atmos. Oceanic Technol.,* **4,** 411–421, doi:10.1175/1520-0426(1987)004<0411:AODFTM>2.0.CO;2.

Iwanami, K., K. Kusunoki, N. Orikasa, M. Maki, R. Misumi, and M. Murakami, 2007: Hydrometeor type classification in winter clouds using X-band polarimetric radar measurements—Comparison of X-band polarimetric radar data with in-situ measurements by HYVIS. Preprints, *33rd Conf. on Radar Meteorology,* Cairns, QLD, Australia, Amer. Meteor. Soc.,

P10.11. [Available online at http://ams.confex.com/ams/pdfpapers/123072.pdf.]

Jaffrain, J., and A. Berne, 2011: Experimental quantification of the sampling uncertainty associated with measurements from PARSIVEL disdrometers. *J. Hydrometeor.,* **12,** 352–370, doi:10.1175/2010JHM1244.1.

Kanofsky, L., and P. B. Chilson, 2008: An analysis of errors in drop size distribution retrievals and rain bulk parameters with a UHF wind profiling radar and a two-dimensional video disdrometer. *J. Atmos. Oceanic Technol.,* **25,** 2282–2292, doi:10.1175/2008JTECHA1061.1.

Knight, N. C., 1986: Hailstone shape factor and its relationship to radar interpretation of hail. *J. Climate Appl. Meteor.,* **25,** 1956–1958, doi:10.1175/1520-0450(1986)025<1956:HSFAIR>2.0.CO;2.

——, and A. J. Heymsfield, 1983: Measurement and interpretation of hailstone density and terminal velocity. *J. Atmos. Sci.,* **40,** 1510–1516, doi:10.1175/1520-0469(1983)040<1510:MAIOHD>2.0.CO;2.

Kruger, A., and W. F. Krajewski, 2002: Two-dimensional video disdrometer: A description. *J. Atmos. Oceanic Technol.,* **19,** 602–617, doi:10.1175/1520-0426(2002)019<0602:TDVDAD>2.0.CO;2.

Kwiatkowski, J. M., A. B. Kostinski, and A. R. Jameson, 1995: The use of optimal polarizations for studying the microphysics of precipitation: Nonattenuating wavelengths. *J. Atmos. Oceanic Technol.,* **12,** 96–114, doi:10.1175/1520-0426(1995)012<0096:TUOOPF>2.0.CO;2.

Lesins, G. B., and R. List, 1986: Sponginess and drop shedding of gyrating hailstones in a pressure-controlled icing wind tunnel. *J. Atmos. Sci.,* **43,** 2813–2825, doi:10.1175/1520-0469(1986)043<2813:SADSOG>2.0.CO;2.

Liu, H., and V. Chandrasekar, 2000: Classification of hydrometeors based on polarimetric radar measurements: Development of fuzzy logic and neuro-fuzzy systems, and in situ verification. *J. Atmos. Oceanic Technol.,* **17,** 140–164, doi:10.1175/1520-0426(2000)017<0140:COHBOP>2.0.CO;2.

Locatelli, J. D., and P. Hobbs, 1974: Fall speed and masses of solid precipitation particles. *J. Geophys. Res.,* **79,** 2185–2197, doi:10.1029/JC079i015p02185.

Löffler-Mang, M., and J. Joss, 2000: An optical disdrometer for measuring size and velocity of hydrometeors. *J. Atmos. Oceanic Technol.,* **17,** 130–139, doi:10.1175/1520-0426(2000)017<0130:AODFMS>2.0.CO;2.

——, and U. Blahak, 2001: Estimation of the equivalent radar reflectivity factor from measured snow size spectra. *J. Appl. Meteor.,* **40,** 843–849, doi:10.1175/1520-0450(2001)040<0843:EOTERR>2.0.CO;2.

Markowski, P. M., J. M. Straka, and E. N. Rasmussen, 2002: Direct surface thermodynamic observations within the rear-flank downdrafts of nontornadic and tornadic supercells. *Mon. Wea. Rev.,* **130,** 1692–1721, doi:10.1175/1520-0493(2002)130<1692:DSTOWT>2.0.CO;2.

Nešpor, V., W. F. Krajewski, and A. Kruger, 2000: Wind-induced error of raindrop size distribution measurement using a two-dimensional video disdrometer. *J. Atmos. Oceanic Technol.,* **17,** 1483–1492, doi:10.1175/1520-0426(2000)017<1483:WIEORS>2.0.CO;2.

Palmer, R., and Coauthors, 2009: Weather radar education at the University of Oklahoma—An integrated interdisciplinary approach. *Bull. Amer. Meteor. Soc.,* **90,** 1277–1282, doi:10.1175/2009BAMS2738.1.

Park, H., A. V. Ryzhkov, D. S. Zrnić, and K. Kim, 2009: The hydrometeor classification algorithm for the polarimetric WSR-88D: Description and application to an MCS. *Wea. Forecasting,* **24,** 730–748, doi:10.1175/2008WAF2222205.1.

Park, S. G., V. N. Bringi, V. Chandrasekar, M. Maki, and K. Iwanami, 2005: Correction of radar reflectivity and differential reflectivity for rain attenuation at X band. Part I: Theoretical and empirical basis. *J. Atmos. Oceanic Technol.,* **22,** 1621–1632, doi:10.1175/JTECH1803.1.

Rasmussen, R. M., and A. J. Heymsfield, 1987: Melting and shedding of graupel and hail. Part I: Model physics. *J. Atmos. Sci.,* **44,** 2754–2763, doi:10.1175/1520-0469(1987)044<2754:MASOGA>2.0.CO;2.

Rinehart, R. E., 2004: *Radar for Meteorologists.* Rinehart Publications, 482 pp.

Ryzhkov, A. V., and D. S. Zrnić, 2007: Depolarization in ice crystals and its effect on radar polarimetric measurements. *J. Atmos. Oceanic Technol.,* **24,** 1256–1267, doi:10.1175/JTECH2034.1.

——, M. Pinsky, A. Pokrovsky, and A. Khain, 2011: Polarimetric radar observation operator for a cloud model with spectral microphysics. *J. Appl. Meteor. Climatol.,* **50,** 873–894, doi:10.1175/2010JAMC2363.1.

——, M. R. Kumjian, S. M. Ganson, and A. P. Khain, 2013a: Polarimetric radar characteristics of melting hail. Part I: Theoretical simulations using spectral microphysical modeling. *J. Appl. Meteor. Climatol.,* **52,** 2849–2870, doi:10.1175/JAMC-D-13-073.1.

——, ——, ——, and P. Zhang, 2013b: Polarimetric radar characteristics of melting hail. Part II: Practical implications. *J. Appl. Meteor. Climatol.,* **52,** 2871–2886, doi:10.1175/JAMC-D-13-074.1.

Schuur, T. J., A. V. Ryzhkov, D. S. Zrnić, and M. Schönhuber, 2001: Drop size distributions measured by a 2D video disdrometer: Comparison with dual-polarization radar data. *J. Appl. Meteor.,* **40,** 1019–1034, doi:10.1175/1520-0450(2001)040<1019:DSDMBA>2.0.CO;2.

Sevruk, B., 1982: Methods of correction for systematic error in point precipitation measurement for operational use. Operational Hydrology Rep. 21, Publ. 589, 91 pp. [Available from WMO, Case Postale 2300, CH-1211, Geneva, Switzerland.]

Shabbott, C. J., and P. M. Markowski, 2006: Surface in situ observations within the outflow of forward-flank down drafts of supercell thunderstorms. *Mon. Wea. Rev.,* **134,** 1422–1441, doi:10.1175/MWR3131.1.

SIGMET, 2009: Vaisala user's manual: Digital IF receiver/Doppler signal processor RVP8. SIGMET, 451 pp. [Available online at ftp://ftp.sigmet.com/outgoing/manuals/RVP8_Users_Manual.pdf.]

Snyder, J. C., H. B. Bluestein, G. Zhang, and S. J. Frasier, 2010: Attenuation correction and hydrometeor classification of high-resolution, X-band, dual-polarized mobile radar measurements in severe convective storms. *J. Atmos. Oceanic Technol.,* **27,** 1979–2001, doi:10.1175/2010JTECHA1356.1.

Solheim, F. S., R. Vivekanandan, R. H. Ware, and C. Rocken, 1999: Propagation delays induced in GPS signals by dry air, water vapor, hydrometeors, and other particulates. *J. Geophys. Res.,* **104,** 9663–9670, doi:10.1029/1999JD900095.

Steiner, M., G. Lee, S. M. Ellis, and J. Vivekanandan, 2009: Quantitative precipitation estimation and hydrometeor identification using dual-polarization radar—Phase II. NCAR Tech. Rep., 74 pp. [Available online at ftp://ftp.eol.ucar.edu/pub/temp/users/sellis/Steiner_etal_2009/2009%20KMA-NIMR%20Report.pdf.]

Straka, J. M., 2009: *Cloud and Precipitation Microphysics: Principles and Parameterizations.* Cambridge University Press, 406 pp.

Tabary, P., G. Vulpiani, J. J. Gourley, A. J. Illingworth, and O. Bousquet, 2009: Unusually high differential attenuation at C band: Results from a two-year analysis of the French Trappes polarimetric radar data. *J. Appl. Meteor. Climatol.,* **48,** 2037–2053, doi:10.1175/2009JAMC2039.1.

Testud, J., E. Le Bouar, E. Obligis, and M. Ali-Mehenni, 2000: The rain profiling algorithm applied to polarimetric weather radar. *J. Atmos. Oceanic Technol.,* **17,** 332–356, doi:10.1175/1520-0426(2000)017<0332:TRPAAT>2.0.CO;2.

Thomson, A. D., and R. List, 1996: Raindrop spectra and updraft determination by combining Doppler radar and disdrometer. *J. Atmos. Oceanic Technol.,* **13,** 465–476, doi:10.1175/1520-0426(1996)013<0465:RSAUDB>2.0.CO;2.

Thurai, M., and V. N. Bringi, 2005: Drop axis ratios from a 2D video disdrometer. *J. Atmos. Oceanic Technol.,* **22,** 966–978, doi:10.1175/JTECH1767.1.

——, M. Szakall, V. N. Bringi, K. V. Beard, S. K. Mitra, and S. Borrmann, 2009: Drop shapes and axis ratio distributions: Comparisons between 2D video disdrometer and wind tunnel measurements. *J. Atmos. Oceanic Technol.,* **26,** 1427–1432, doi:10.1175/2009JTECHA1244.1.

——, W. A. Petersen, and L. D. Carey, 2010: DSD characteristics of a cool-season tornadic storm using C-band polarimetric radar and two 2D-video disdrometers. *Proc. Sixth European Conf. on Radar Meteorology and Hydrology,* Sibiu, Romania, European Meteorological Society, 1–6. [Available online at http://www.erad2010.org/pdf/oral/tuesday/radpol1/5_ERAD2010_0101.pdf.]

——, ——, A. Tokay, C. Schultz, and P. Gatlin, 2011: Drop size distribution comparisons between PARSIVEL and 2-D video disdrometers. *Adv. Geosci.,* **30,** 3–9, doi:10.5194/adgeo-30-3-2011.

Ulbrich, C. W., and N. E. Miller, 2001: Experimental test of the effects of *Z–R* law variations on comparison of WSR-88D rainfall amounts with surface rain gauge and disdrometer data. *Wea. Forecasting,* **16,** 369–375, doi:10.1175/1520-0434(2001)016<0369:ETOTEO>2.0.CO;2.

Vivekanandan, J., W. M. Adams, and V. N. Bringi, 1991: Rigorous approach to polarimetric radar modeling of hydrometeor distributions. *J. Appl. Meteor.,* **30,** 1053–1063, doi:10.1175/1520-0450(1991)030<1053:RATPRM>2.0.CO;2.

——, R. Raghavan, and V. N. Bringi, 1993: Polarimetric radar modeling of mixtures of precipitation particles. *IEEE Trans. Geosci. Remote Sens.,* **31,** 1017–1030, doi:10.1109/36.263772.

——, S. M. Ellis, R. Oye, D. S. Zrnić, A. V. Ryzhkov, and J. Straka, 1999: Cloud microphysics retrieval using S-band dual-polarization radar measurements. *Bull. Amer. Meteor. Soc.,* **80,** 381–388, doi:10.1175/1520-0477(1999)080<0381:CMRUSB>2.0.CO;2.

Vulpiani, G., P. Tabary, J. Parent du Chatelet, and F. Marzano, 2008: Comparison of advanced radar polarimetric techniques for operational attenuation correction at C band. *J. Atmos. Oceanic Technol.,* **25,** 1118–1135, doi:10.1175/2007JTECHA936.1.

Wurman, J., D. Dowell, Y. Richardson, P. Markowski, E. Rasmussen, D. Burgess, L. Wicker, and H. Bluestein, 2012: The second Verification of the Origins of Rotation in Tornadoes Experiment: VORTEX2. *Bull. Amer. Meteor. Soc.,* **93,** 1147–1170, doi:10.1175/BAMS-D-11-00010.1.

Yuter, S. E., D. E. Kingsmill, L. B. Nance, and M. Loffler-Mang, 2006: Observations of precipitation size and fall speed characteristics within coexisting rain and wet snow. *J. Appl. Meteor. Climatol.,* **45,** 1450–1464, doi:10.1175/JAM2406.1.

Zhang, G., S. Luchs, A. V. Ryzhkov, M. Xue, L. Ryzhkova, and Q. Cao, 2011: Winter precipitation microphysics characterized by polarimetric radar and video disdrometer observations in central Oklahoma. *J. Appl. Meteor. Climatol.,* **50,** 1558–1570, doi:10.1175/2011JAMC2343.1.

Zrnić, D. S., R. J. Doviak, G. Zhang, and A. V. Ryzhkov, 2010: Bias in differential reflectivity due to cross-coupling through the radiation patterns of polarimetric weather radars. *J. Atmos. Oceanic Technol.,* **27,** 1624–1637, doi:10.1175/2010JTECHA1350.1.